



### **Science Arts & Métiers (SAM)**

is an open access repository that collects the work of Arts et Métiers Institute of Technology researchers and makes it freely available over the web where possible.

This is an author-deposited version published in: <https://sam.ensam.eu>  
Handle ID: <http://hdl.handle.net/10985/21521>

#### **To cite this version :**

T. LAVIGNE, Giuseppe SCIUMÈ, Stéphane URCUN, B. WHEATLEY, Sébastien LAPORTE, Pierre-Yves ROHAN, Helene PILLET - Numerical investigation of the time-dependent stress-strain mechanical behaviour of skeletal muscle tissue in the context of pressure ulcer prevention - Clinical Biomechanics p.105592 - 2022

Any correspondence concerning this service should be sent to the repository

Administrator : [scienceouverte@ensam.eu](mailto:scienceouverte@ensam.eu)



14 Numerical investigation of the time-dependent  
15 stress-strain mechanical behaviour of skeletal muscle  
16 tissue in the context of Pressure Ulcer prevention

17 T. Lavigne<sup>a,b,\*</sup>, G. Sciumè<sup>b</sup>, S. Laporte<sup>a</sup>, H. Pillet<sup>a</sup>, S. Urcun<sup>a,b,c</sup>, B.  
18 Wheatley<sup>d</sup>, P-Y. Rohan<sup>a</sup>

<sup>a</sup>*Arts et Metiers Institute of Technology, IBHGC, 151 bd de  
l'hôpital, Paris, 75013, France*

<sup>b</sup>*Arts et Metiers Institute of Technology, Univ. of Bordeaux, CNRS, Bordeaux INP,  
INRAE, I2M Bordeaux, Avenue d'Aquitaine, Pessac, 33607, France*

<sup>c</sup>*Institute for Computational Engineering Sciences, Department of Engineering Sciences,  
Faculte des Sciences, de la Technologie et de Medecine, Universite du  
Luxembourg, Campus Kirchberg, 6, rue*

*Coudenhove-Kalergi, Luxembourg, L-1359, Luxembourg*

<sup>d</sup>*Department of Mechanical Engineering, Bucknell University, 1 Dent  
Drive, Lewisburg, 17837, Pennsylvania, USA*

---

19 **Abstract**

20 *Background:* Pressure-induced tissue strain is one major pathway for Pres-  
21 sure Ulcer development and, especially, Deep Tissue Injury. Biomechanical  
22 investigation of the time-dependent stress-strain mechanical behaviour of  
23 skeletal muscle tissue is therefore essential to understand and prevent the  
24 onset of Deep Tissue Injury. In the literature, a viscoelastic formulation is  
25 generally assumed for the experimental characterization of skeletal muscles,  
26 with the limitation that the underlying physical mechanisms that give rise  
27 to the time dependent stress-strain behaviour are not known. The objective  
28 of this study is to explore the capability of poroelasticity to reproduce the  
29 apparent viscoelastic behaviour of passive muscle tissue under confined com-  
30 pression.

31 *Methods:* Experimental stress-relaxation response of 31 cylindrical porcine  
32 samples tested under fast and slow confined compression by Vaidya and col-  
33 laborators were used. An axisymmetric Finite Element model was developed  
34 in ABAQUS and, for each sample a one-to-one inverse analysis was per-  
35 formed to calibrate the specimen-specific constitutive parameters, namely,  
36 the drained Young's modulus, the void ratio, hydraulic permeability, the



37 Poisson's ratio, the solid grain's and fluid's bulk moduli.

38 *Findings:* The peak stress and consolidation were recovered for most of the  
39 samples (N=25) by the poroelastic model (normalised root-mean-square er-  
40 ror  $\leq 0.03$  for fast and slow confined compression conditions).

41 *Interpretation:* The strength of the proposed model is its fewer number of  
42 variables (N=6 for the proposed poroelastic model versus N=18 for the vis-  
43 cohypereelastic model proposed by Vaidya and collaborators). The incorpo-  
44 ration of poroelasticity to clinical models of Pressure Ulcer formation could  
45 lead to more precise and mechanistic explorations of soft tissue injury risk  
46 factors.

47 *Keywords:* pressure ulcer, load-tolerant soft tissues, muscle passive  
48 behaviour, viscoelasticity, poroelasticity

---

49 **Count of words. Abstract: 260; Manuscript: 3611.**

## 50 1. Introduction

51 Pressure Ulcers (PUs) have been defined in the 2019 Clinical Practice  
52 Guideline (CPG) published jointly by the European Pressure Ulcer Advisory  
53 Panel (EPUAP), the National Pressure Injury Advisory Panel (NPIAP), and  
54 the Pan Pacific Pressure Injury Alliance (PPPIA) as "*localized injuries to the*  
55 *skin and underlying soft tissue that form during prolonged exposure to me-*  
56 *chanical loads*" (Gefen et al. [1]). These usually occur over a bony prominence  
57 but may also be related to the interaction between the skin and an external  
58 medical device such as, for example, when patients interact with medical  
59 devices (orthoses, prostheses, manual wheelchair, etc) or support surfaces  
60 (Gefen et al. [2]). Despite long-standing risk assessment scales and man-  
61 agement strategies, the relative high incidence of PUs, **and especially Deep**  
62 **Tissue Injuries (DTI)**, requires extensive treatment representing a significant  
63 financial burden on health services throughout the world (Bennett et al. [3]).

64 Over the past 20 years, research has sought to explain soft tissue in-  
65 jury risk factors in terms of the local mechanical environment within soft  
66 tissues. Of particular interest are the series of experiments performed at  
67 the Eindhoven University of Technology (Ceelen et al. [4], Loerakker et al.

---

\*Corresponding author

*Email address:* thomas.lavigne@ensam.eu (T. Lavigne)

68 [5], Stekelenburg et al. [6], van Nierop et al. [7], Traa et al. [8]) involving  
69 indentation of the tibialis anterior muscle of Brown-Norway rats that lead to  
70 identify a damage threshold for healthy murine skeletal muscle tissue. Using  
71 dedicated organ-scale Finite Element models, it was shown that direct defor-  
72 mation damage was apparent only when a given maximum Green-Lagrange  
73 shear strain threshold was exceeded (Ceelen et al. [4]), and that the dam-  
74 aged area was correlated to the magnitude of the elastic strain energy applied  
75 (Loerakker et al. [9]).

76 To interrogate individual soft tissue injury risk based on the evaluation of  
77 the local mechanical state, tissue-scale Finite Element models of load-bearing  
78 soft tissue in humans have been developed. These have consistently shown  
79 that bony prominence in the buttock (Linder-Ganz et al. [10, 11, 12], Luboz  
80 et al. [13], Moerman et al. [14], Macron et al. [15]), the foot (Bucki et al.  
81 [16], Niroomandi et al. [17], van Zwam et al. [18]) and at the stump-socket  
82 interface (Portnoy et al. [19], Dickinson et al. [20], Ramasamy et al. [21])  
83 induce substantial stress concentrations (generally in skeletal muscles), which  
84 explains why these areas are vulnerable to ulceration.

85 Studies in the literature however are generally conducted with the as-  
86 sumption of quasi-static loading and response (Al-Dirini et al. [22]). Yet, the  
87 knowledge of the local mechanical condition alone is not sufficient to predict  
88 tissue damage initiation. The major limitation is that tissue damage is gov-  
89 erned by a number of coupled biological and physical processes that occur  
90 at different spatial scales and often have very different temporal characteris-  
91 tics. Hence, the loading history is essential, because the time that a tissue is  
92 subjected to a sustained compression is a major determinant of tissue dam-  
93 age. It follows that the biomechanical investigation of the time-dependent  
94 stress-strain mechanical behaviour of soft tissues, and in particular, of skele-  
95 tal muscle tissue, is essential to **improve the understanding of the onset of**  
96 **DTI and therefore would allow a better prevention.**

97 Attempts to characterise the time-dependence of skeletal muscle tissue  
98 generally assume a viscoelastic formulation and typically ignore the bi-phasic  
99 nature of the tissue (Van Looke et al. [23], Simms et al. [24], Wheatley et al.  
100 [25]). In the case of viscoelasticity, the underlying physical mechanisms that  
101 give rise to the time dependent stress-strain behavior are not taken into  
102 account mechanistically. Yet, it is known that skeletal muscles are composed  
103 of a porous solid matrix (muscle fibers and extracellular matrix) filled with  
104 fluid (approximately 75% bound and free fluid Sjogaard and Saltin [26]).  
105 The overall mechanical behavior of these tissues depends not only on the

106 solid matrix deformation, but also on the movement of the fluid within the  
107 pores during the deformation. Since fluid plays a role in the load transfer in  
108 these tissues, it follows that the stress-strain behavior of these tissues will be  
109 time dependent.

110 Many research teams have proposed using poroelastic constitutive mod-  
111 els as an alternative to visco-elastic models to capture the history-dependent  
112 response of soft tissues under static and dynamics loading (Gimnich et al.  
113 [27], Argoubi and Shirazi-Adl [28], Peyrounette et al. [29], Siddique et al.  
114 [30], Hosseini-Farid et al. [31], Franceschini et al. [32], Sciumè et al. [33]).  
115 A comparison between visco-elastic and poro-elastic framework given in Ap-  
116 pendix C. Porous media models also represent a promising approach for  
117 the integration of multiscale/multiphysics data to probe biologically rele-  
118 vant phenomena at a smaller scale and embed the relevant mechanisms at  
119 the larger scale (in particular, biochemistry of oxygen and of inflammatory  
120 signalling pathways), allowing the interpretation of the different time char-  
121 acteristics (Urcun et al. [34], Sciumè et al. [35], Sciumè [36], Gray and Miller  
122 [37], Mascheroni et al. [38]).

123 In a previous study, Vaidya and Wheatley [39] have tested porcine Tibialis  
124 Anterior (TA) muscle samples under fast and slow Confined/Unconfined com-  
125 pression and have proposed a robust hyper-viscoelastic model to numerically  
126 reproduce the mechanical behaviour in compression based on four loading  
127 conditions. Building upon this experimental work, the aim of the presented  
128 study is to explore the capability of poroelasticity to reproduce the apparent  
129 viscoelastic behaviour of passive muscle tissue under Confined Compression  
130 and to investigate the contribution of extracellular fluid flow.

## 131 **2. Methods**

### 132 *2.1. Experimental data*

133 This study was based on the experimental stress relaxation results of  
134 porcine muscle samples tested under fast and slow confined compression  
135 in Vaidya and Wheatley [39] (Figure 1 (a, b, c)). Briefly, thirty-one cylin-  
136 drical muscle porcine samples (average height 7.03 mm and average radius  
137 3.2 mm) were compressed in an impermeable steel well (diameter=6.9 mm,  
138 depth=8 mm), using a uniaxial tabletop Instron 3366 tensile testing system  
139 equipped with an Al<sub>2</sub>O<sub>3</sub> porous plunger (diameter=6.4 mm, length=25.5  
140 mm, Figure 1 (a)). Two stress relaxation testing conditions were used. Spec-  
141 imens were strained to 15% at two different strain rates: a fast compression

142 at  $15\% \text{ s}^{-1}$  (n=16 cylinders) and a slow compression at  $1.5\% \text{ s}^{-1}$  (n=15 cylinders).  
 143 They were maintained at this strain level during 400s (Figure 1 (c)).  
 144 All tests were completed under transverse compression to simulate the most  
 145 common uniaxial physiological loading orientation.

146 A visco-hyper-elastic model was calibrated in Vaidya and Wheatley [39]  
 147 using unconfined and confined fast compression data concurrently. This constitutive  
 148 model was based on an uncoupled Yeoh hyperelastic formulation  
 149 and a four cell Maxwell viscoelastic model (four term Prony series). The  
 150 results obtained are recalled in Table 1.

Law	Parameters Type	Parameter symbol	Value
Yeoh	Hyper-elastic (MPa)	$C_{10}, C_{20}, C_{30}$	$2.23 \cdot 10^{-5}, 1.28 \cdot 10^{-4}, 2.52 \cdot 10^{-5}$
	Hyper-elastic ( $\text{MPa}^{-1}$ )	$D_1, D_2, D_3$	105.9, 0.839, 0.0
Prony Series	Shear Coefficients (-)	$G_1, G_2, G_3, G_4$	0.741, 0.086, 0.093, 0.061
	Bulk Coefficients (-)	$K_1, K_2, K_3, K_4$	0.563, 0.150, 0.108, 0.147
	Time Coefficients (s)	$\tau_1, \tau_2, \tau_3, \tau_4$	0.05, 1, 20, 400

Table 1: Hyper-elastic and viscoelastic parameters of the finite element model calibrated using unconfined and confined fast compression data concurrently [39]

151 The present study focuses on the Confined Compression case, but future  
 152 work will extend the work to the Unconfined Compression case.

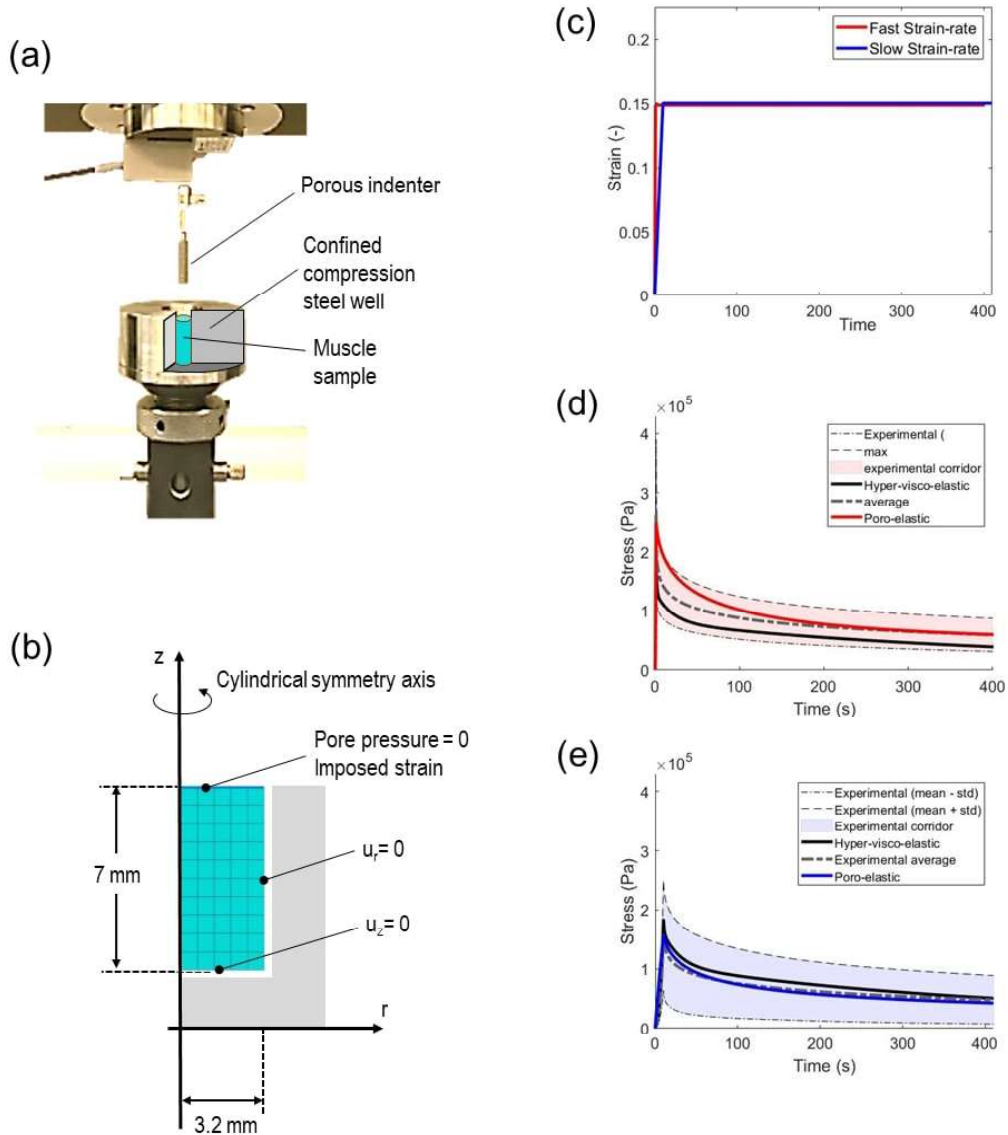


Figure 1: Experimental set up for Confined Compression (a) with its schematic representation of the finite element model (b) and imposed strain law (c) from Vaidya and Wheatley [39]. Results for the fast strain-rate (d) and for the slow strain-rate (e) average experimental relaxation curve calibration. The experimental corridor of the campaign of Vaidya and Wheatley [39] is light red for the fast strain rate and light blue for the slow one, the average experimental stress is in dashed grey. The visco-hyper-elastic model calibrated in Vaidya and Wheatley [39] is in black while poroelastic model predictions with a Poisson's ratio of 0.4879 are in red for the fast strain rate and blue for the slow strain-rate.

153 *2.2. Finite Element Modeling*

154 A poro-elastic mathematical model was implemented in the general pur-  
 155 pose Finite Element software ABAQUS (ABAQUS, 2019) and an inverse  
 156 analysis was performed to fit a quasi-incompressible, isotropic, poroelastic  
 157 constitutive model (solid saturated by an incompressible viscous fluid) to re-  
 158 produce the mean experimental mechanical response (stress relaxation). For  
 159 more details on the theoretical basis of the model, the reader is referred to  
 160 Appendix B. The modelling procedure followed complies with the consensus  
 161 process that started within the Editorial Board of Clinical Biomechanics, and  
 162 published by Viceconti and collaborators Viceconti et al. [40].

163 In this work, inertial and gravitational forces were neglected. It was also  
 164 assumed that there is no blood flux in the samples since the experimentation  
 165 was performed *ex vivo* on small samples. Muscle tissue was therefore assumed  
 166 to be a mixture of two phases, an interstitial fluid and the solid scaffold. The  
 167 porous medium was assumed to be fully saturated.

168 A preliminary study for small deformation case was carried out to assess  
 169 the reliability of our formulation, comparing to the Terzaghi analytic solution  
 170 (see Appendix D).

171 Then, a 2D axisymmetric model was proposed for the Confined Compres-  
 172 sion test (n=50 CAX4PH elements: 4-node bi-linear displacement and pore  
 173 pressure, hybrid with constant pressure), as illustrated in Figure 1 (b).

174 The definition of the constitutive laws was defined as follows. The solid  
 175 phase behaviour was assumed linear elastic (eq. B.11). Hence, it was gov-  
 176 erned by its Young's modulus,  $E$ , and Poisson's ratio,  $\nu$ . The pore fluid was  
 177 assumed to follow Darcy's law as presented before, and was approximated  
 178 by the Forchheimer's law of Abaqus [41] (eq. 1) . Finally, the model was  
 179 completed by the definition of the bulk moduli of solid grain,  $K^s$ , and of the  
 180 fluid,  $K^l$ .

$$s\varepsilon^l \mathbf{v}^l = -\tilde{k} \cdot \left( \frac{\partial \mathbf{p}}{\partial \mathbf{x}} \right) \quad (1)$$

$$\tilde{k} = \frac{k^\varepsilon}{\mu^l} \quad (2)$$

181 Where  $\tilde{k}$  denotes the hydraulic permeability depending on the void ratio,  $e = \frac{\varepsilon^l}{1-\varepsilon^l}$ .  $\mathbf{v}^l$  is  
 182 the fluid velocity. Finally,  $p$  is the wetting liquid pore pressure,  $s$  the fluid saturation of  
 183 the porous medium.

184 Boundary conditions are recalled in Figure 1 (b). As it was defined in the  
185 previous section, two types of boundary conditions were defined. Displace-  
186 ment BC were imposed on the top surface at the several strain rates. A pore  
187 pressure equal to zero was imposed on the fluid leaking surfaces. Displace-  
188 ment was vertically locked on the bottom surface and radially locked on the  
189 lateral surface.

190 Once the material was defined, three analysis steps were created. Dur-  
191 ing the first step, only the displacement boundary conditions were defined.  
192 Additionally, an initial void ratio of the porous medium was defined. Then,  
193 the displacement load was applied during a compression step, and the pore  
194 pressure boundary condition was added. Finally, the imposed displacement  
195 was sustained so as to observe the stress relaxation during 400s. For these  
196 two last steps, the soil formulation proposed by ABAQUS was used with an  
197 iterative resolution scheme due to the high strains. The duration of the steps  
198 were provided according to Vaidya and Wheatley [39] experiments and an  
199 automatic time step was considered.

### 200 2.3. Model Calibration

201 The mean experimental stress relaxation curve of confined compression  
202 were fitted using the `@lsqnonlin()` function of Matlab (Matlab R2019a) and  
203 its 'Trust-reflective' algorithm. Specifically, we used Matlab to call ABAQUS  
204 with an initial **estimate** for the material model parameters, performed a for-  
205 ward simulation in ABAQUS, read the simulation-based output forces in  
206 Matlab, computed a custom error metric  $J$  (eq. 6) computing the error over  
207 the peak stress (eq. 3), the area between the curves (eq. 5) and the final slope  
208 of the curve (eq. 4) (over the 50 last seconds). This process was repeated  
209 iteratively until reaching the cost function local minimum.

210 As the algorithm 'Trust-region-reflective' of the least square minimisation  
211 function is based over gradients, it is more sensitive to the initial **estimate**,  
212 and a high number of parameters increase the risks of local minimums. A  
213 preliminary calibration was therefore run over the averaged stress-time exper-  
214 imental curve considering the 6 parameters of our model ( $E$ ,  $\nu$ ,  $e$ ,  $\tilde{k}$ ,  $K^s$ ,  $K^l$ ).  
215 In order to minimize the risk of local minimums during the calibration proce-  
216 dure, the following parameters were assigned the value obtained during this  
217 preliminary calibration :  $\nu = 0.4879$  and  $K^s = 0.799\text{MPa}$ .  $K^l = 2.2\text{GPa}$  was  
218 assumed to be equal to the water bulk modulus. The one-to-one calibration  
219 was therefore performed on the following subset of parameters :  $E$ ,  $e$ ,  $\tilde{k}$ .

$$J_1 = \frac{1}{3} \cdot \left( \frac{\max(\mathbf{t}_{abq}^{tot}) - \max(\mathbf{t}_{exp}^{tot})}{\max(\mathbf{t}_{exp}^{tot})} \right)^2 \quad (3)$$

$$J_2 = \frac{1}{3} \cdot \left( \frac{\frac{\partial \mathbf{t}_{abq}^{tot}}{\partial t} - \frac{\partial \mathbf{t}_{exp}^{tot}}{\partial t}}{\frac{\partial \mathbf{t}_{exp}^{tot}}{\partial t}} \right)^2 \quad (4)$$

$$J_3 = \frac{1}{3} \cdot \left( \frac{rms(\mathbf{t}_{abq}^{tot} - \mathbf{t}_{exp}^{tot})}{norm(\mathbf{t}_{exp}^{tot})} \right)^2 \quad (5)$$

$$J = J_1 + J_2 + J_3 \quad (6)$$

220 Where  $\mathbf{t}_{abq}^{tot}$  is the stress-time solution of ABAQUS,  $\mathbf{t}_{exp}^{tot}$  is the experimental stress-time  
 221 curve,  $\frac{\partial \bullet}{\partial t}$  is the derivative over the last points of the data,  $rms()$  and  $norm()$  are respec-  
 222 tively the root mean square and norm functions of matlab.

223 The samples' size, '.inp' ABAQUS files and python routines for ABAQUS  
 224 are provided to the reader in Appendix A.

### 225 3. Results

#### 226 3.1. Sensitivity to mesh and initial *estimate*

227 A mesh analysis was conducted. Due to the simplicity of the geometry  
 228 of the sample, little variation was observed depending on the seeding. Three  
 229 seeding were considered: 50 dof, 105 dof and 180 dof. These different seeding  
 230 of the mesh led to negligible change in the mechanical response (quantita-  
 231 tively, the cost function was unchanged and equal to 0.0061).

232 Another sensitivity study was carried out over the initial parameter *esti-*  
 233 *mates*. Two initial *estimates* have been considered for the Young's mod-  
 234 ulus  $E$ , void ratio  $e$  and hydraulic permeability  $\tilde{k}$ : [ $E = 17989\text{Pa}, e =$   
 235  $0.6996, \tilde{k} = 6.07 \cdot 10^{-14}\text{m}^2 \text{Pa}^{-1} \text{s}^{-1}$ ] *vs.* [ $E = 8995\text{Pa}, e = 0.3498, \tilde{k} =$   
 236  $3.035 \cdot 10^{-14}\text{m}^2 \text{Pa}^{-1} \text{s}^{-1}$ ]. The error metrics varied between 0.0061 and 0.0084  
 237 respectively. This difference of the cost function is discussed in the section  
 238 4.

#### 239 3.2. Calibration of the average experimental relaxation curve

240 The result of the calibration of the average relaxation stress-time curve is  
 241 superimposed in Figure 1 (d, e) onto the average experimental sample stress-  
 242 time curve and the experimental corridor. The calibrated visco-hyper-elastic



243 numerical model reported in Vaidya and Wheatley [39] is also superimposed  
 244 for the ease of comparison.

245 The parameters identified were, respectively, for fast and slow strain-  
 246 rate: Young’s modulus of 22 kPa, Poisson’s ratio of 0.4879, void ratio  $e$  of  
 247 0.85 (which corresponds to a porosity of 46%) and hydraulic permeability of  
 248  $\tilde{k} = 4.49 \cdot 10^{-14} \text{ m}^2 \text{ Pa}^{-1} \text{ s}^{-1}$ ; Young’s modulus of 5.77 kPa, Poisson’s ratio  
 249 of 0.4879, void ratio  $e$  of 0.64 (which corresponds to a porosity of 39%) and  
 250 hydraulic permeability of  $\tilde{k} = 2.33 \cdot 10^{-14} \text{ m}^2 \text{ Pa}^{-1} \text{ s}^{-1}$ .

251 Quantitative error metrics of the optimisation procedure for the proposed  
 252 poroelastic model are reported in Table 2. The different components of the  
 253 cost function are reported, namely  $J_1$  (eq. 3) (peak stress error),  $J_2$  (eq.  
 254 4) (end slope error),  $J_3$  (eq. 5) (normalised root mean square error) and  $J$   
 255 (eq. 6) (cost function). These metrics were also assessed on the numerical  
 256 curves stress-time curve fitted with the visco-hyper-elastic model in Vaidya  
 257 and Wheatley [39] and reported in the table for comparison. The cost func-  
 258 tion between the optimised poroelastic numerical curve and the experimental  
 259 curve is smaller with the proposed poroelastic model than with the visco-  
 260 hyper-elastic model in Vaidya and Wheatley [39] (0.0016 versus 0.21 for the  
 261 slow and 0.0061 versus 0.2477 for the fast).

Model	Strain-rate	$J_1$ (eq. 3)	$J_2$ (eq. 4)	$J_3$ (eq. 5)	$J$ (eq. 6)
Uncoupled Yeoh/Prony visco-hyper-elastic	Slow	0.0283	0.5936	0.0081	0.21
	Fast	0.1559	0.4611	0.0046	0.2477
Poro-linear-elastic Current study	Slow	0.00005	0.00079	0.0039	0.0016
	Fast	0.0026	0.0092	0.007	0.0061

Table 2: Error metrics of the average experimental stress calibrated models for the fast and slow strain-rates of the model proposed by Vaidya and Wheatley [39] and the current study’s model

### 262 3.3. One to one sample calibration

263 The one to one calibration was carried out on  $n=15$  samples (numbered  
 264 1 to 15) for the slow strain-rate loading condition and on  $n=16$  samples  
 265 (numbered 16 to 31) for the fast strain-rate loading condition. The corre-  
 266 sponding stress-time curves for each sample are reported in Figures 2 and 3  
 267 respectively for the slow and for the fast loading rates. Visually inspecting  
 268 the 31 calibrated curves, it can be observed that most of the samples are  
 269 not fully consolidated at the end time of the experiments as the respective  
 270 slope is non-zero. The calibration procedure allowed to approximate the

271 slope between 350 s and 400 s with a poro-elastic model for all the samples  
272 (important because all the samples were not necessarily fully consolidated  
273 experimentally at 400 s). Also, the peak stress is mostly recovered by the  
274 poroelastic model (N=25/31 for which the difference between the peak stress  
275 assessed experimentally and that predicted by the simulation is lower than  
276 5 %).

Solid Phase		Fluid Phase			Error Metrics		
Linear Elastic Law	Soil Grain Bulk Modulus	Darcy's Law	Fluid Bulk Modulus	Total	Peak Stress	Slope	RMS
$E$ (kPa)	$K^s$ (MPa)	$k$ ( $\text{m}^2 \text{Pa}^{-1} \text{s}^{-1}$ )	$K^r$ (MPa)	$J$ (eq. 6)	$J_1$ (eq. 3)	$J_2$ (eq. 4)	$J_3$ (eq. 5)
$12.89 \pm 11.29$	$0.799$	$2.09 \cdot 10^{-13} \pm 3.12 \cdot 10^{-13}$	$2200$	$0.0279 \pm 0.0461$	$0.0175 \pm 0.0285$	$0.0470 \pm 0.1244$	$0.0194 \pm 0.0174$
$20.16 \pm 8.54$	$0.799$	$1.94 \cdot 10^{-13} \pm 5.71 \cdot 10^{-13}$	$2200$	$0.0523 \pm 0.1094$	$0.0213 \pm 0.0429$	$0.1005 \pm 0.2582$	$0.0181 \pm 0.0188$

Table 3: Calibrated parameters and error metrics: mean and standard deviation. First line corresponds to slow-rate parameters and second line to fast-rate results

277 Table 3 provides the mean and standard deviation of the calibrated pa-  
278 rameters. The parameters obtained by calibration per sample are given Ap-  
279 pendix A. The same order of magnitude is obtained whether the strain-rate  
280 was fast or slow. The measured error metrics (eq. 6) of the calibration were  
281 respectively  $0.0523 \pm 0.1094$  and  $0.0279 \pm 0.0461$  (mean and standard devia-  
282 tion of all error metrics are provided Table 3). To quantify the goodness of  
283 fit, the value of the cost function value at the solution  $\mathbf{J}_{final}^{tot}$  is given for each  
284 sample in figure 4 below.

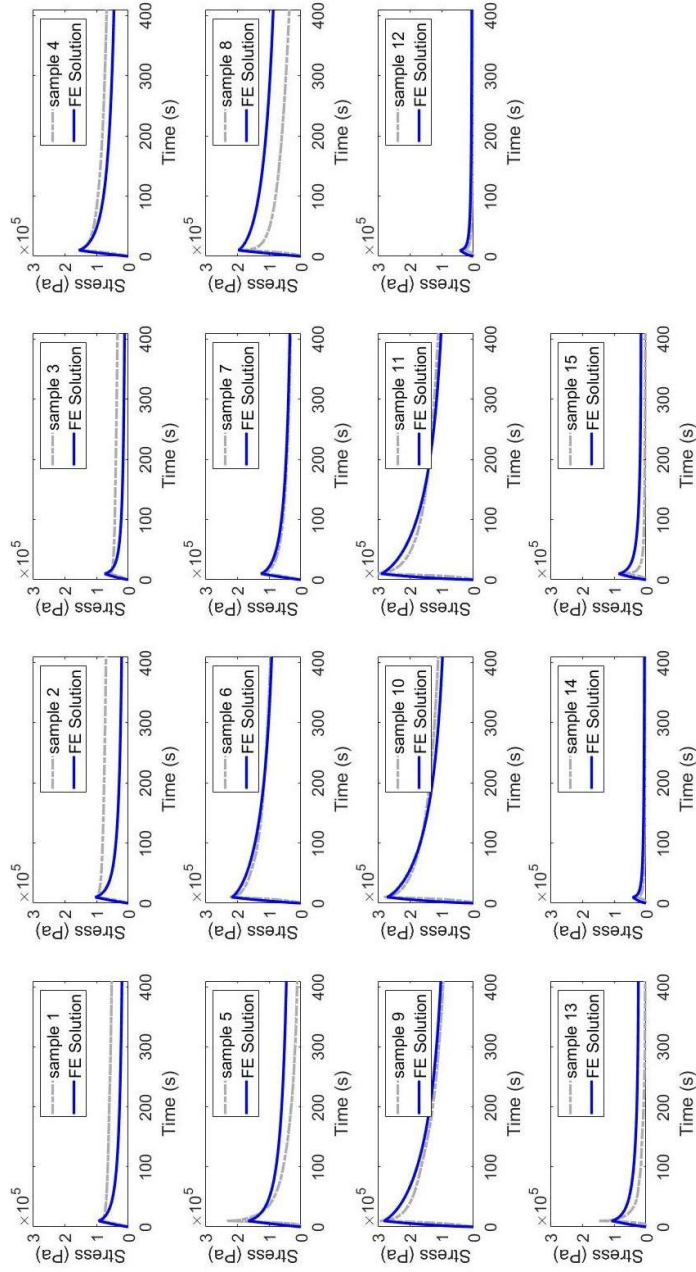


Figure 2: All 15 FE calibrated numerical solutions (blue) superimposed onto the corresponding experimental data (dashed light grey) for slow rate experiments.

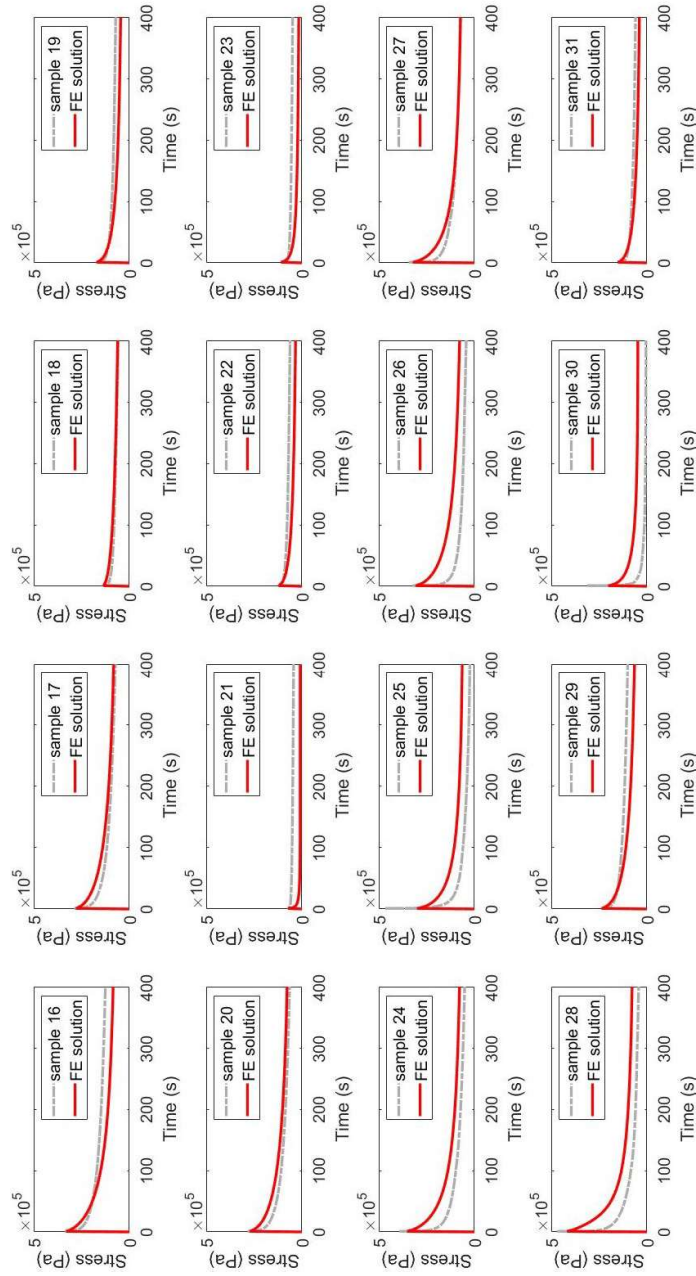


Figure 3: All 16 samples FE calibrated numerical solutions (red) superimposed onto the corresponding experimental data (dashed light grey) for fast rate experiments.

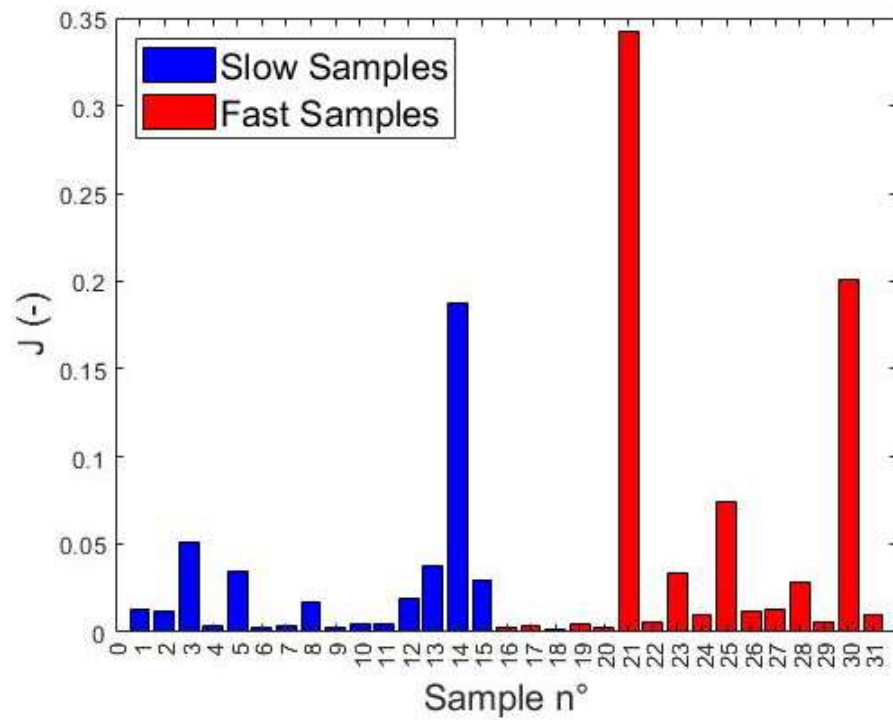


Figure 4: Cost function value at the solution for each sample. Blue corresponds to samples tested with a slow strain-rate loading and red to the samples tested with fast strain-rate loading. The proposed cost function combines the error over the peak stress, the area between the curves and the final slope (over the 50 last seconds). The cost function at the end of the identification was higher for sample 14, 21 and 30. These samples were probably already partially drained as a result of the sample preparation protocol. Hence, the assumption of full saturation might be a strong assumption.

## 285 4. Discussion

286 Biomechanical investigations of the time-dependent stress-strain mechan-  
287 ical behaviour of skeletal muscle tissue is essential to understand and proac-  
288 tively prevent Pressure Ulcer formation. Yet, in the literature, a viscoelastic  
289 formulation is generally assumed for the experimental characterisation of  
290 skeletal muscles, with the limitation that the underlying physical mecha-  
291 nisms that give rise to the time dependent stress-strain behaviour are not  
292 modelled explicitly. The objective of this study has been to explore the  
293 capability of poroelasticity to reproduce the apparent viscoelastic behaviour  
294 of passive muscle tissue under confined compression and to investigate the  
295 contribution of extracellular fluid flow. The peak stress and consolidation  
296 were recovered for most of the samples (N=25/31) by the poroelastic model  
297 (normalised root-mean-square error  $\leq 0.03$  for fast and slow confined com-  
298 pression conditions).

299 Two strong modelling assumptions have been made for drained solid  
300 phase in this work: it was assumed to be both quasi-incompressible and  
301 linear elastic. The assumption of a quasi-incompressible drained solid phase  
302 seems reasonable because muscle fibres may exhibit nearly incompressible  
303 behaviour as fluid-filled structures with no fluid transport across the cell  
304 boundary. There is evidence that this is the case ( Sleboda and Roberts  
305 [42]) and previous modeling work of muscle tissue as a multi-phase material  
306 utilized a solid phase Poisson's ratio of 0.4 ( Wheatley et al. [43]). If the  
307 drained solid phase was assumed to be highly compressible, this would lead  
308 to a different set of calibrated constitutive poro-elastic parameters (the reader  
309 is referred to appendix F) strongly suggesting that further experimental and  
310 theoretical investigations are needed to shed more light on the mechanical  
311 behaviour of the drained solid scaffold.

312 The assumption that a linear elastic model can be used to approximate  
313 the mechanical response of the drained solid phase up to 15% of global com-  
314 pression is indeed a strong one considering that many studies in the literature  
315 reproduce the finite deformation of soft tissues in compression in the context  
316 of Pressure Ulcer prevention using a hyper-elastic constitutive formulation  
317 ( Al-Dirini et al. [22], Moerman et al. [14], Oomens et al. [44], Traa et al.  
318 [45], Lee et al. [46], Verver et al. [47], Levy et al. [48], Linder-Ganz et al.  
319 [11], Sopher et al. [49], Zeevi et al. [50]). Yet, as demonstrated in appendix  
320 E, the hyper-elastic constitutive formulations assumed in the literature gen-  
321 erally result in a quasi-linear stress versus strain behaviour in compression.



322 These results are also consistent with the results reported in Gras et al.  
 323 [51] which provides evidences that a linear elastic model can be used to  
 324 correctly approximate the mechanical response of tissues in confined com-  
 325 pression (without fluid leakage). These also suggest that the main sources  
 326 of non-linearities mostly come from the geometry of the samples. The large  
 327 spread of estimated values of Young's modulus obtained with two loading  
 328 conditions (fast or slow rate) can most probably be explained by the ill-  
 329 posed nature of the inverse problem defined in this study (there is no unique  
 330 solution). Future perspective work will focus on fitting stress relaxation data  
 331 of muscle in both Confined Compression and Unconfined Compression.

332 The strength of the poroelastic model assumed in this study is the fact  
 333 that we model mechanistically the phenomenon that induce the time-dependent  
 334 behavior: i.e. drainage. Also, the model has a lower number of constitutive  
 335 parameters compared to more complex constitutive models employed in the  
 336 literature to capture the temporal evolution of muscle tissue. For example,  
 337 the visco-hyper-elastic model assumed in Vaidya and Wheatley [39] has 18  
 338 parameters to calibrate versus 6 parameters in the present study: the Young's  
 339 modulus and Poisson's ratio of the drained solid matrix, the void ratio and  
 340 hydraulic permeability of the sample, and the soil grain's and fluid's bulk  
 341 moduli. As it was the case in most of the previous studies cited, we assessed  
 342 a macroscopic quasi-incompressible behaviour for the solid scaffold with a  
 343 Poisson's ratio fixed to 0.4879. The identified Young's modulus were on av-  
 344 erage of  $16.63 \pm 10.48 \text{kPa}$  (min: 2kPa; max: 31.19kPa) for both fast and slow  
 345 rate experiments.

346 Few poroelastic models were previously proposed for the muscle - most of  
 347 them used the poroelastic framework to model the mechanical behaviour of  
 348 cartilage (Klika et al. [52]) and bone (Cowin [53], Hellmich and Ulm [54]). In  
 349 experiments carried out over four New Zealand White Rabbits biceps femoris  
 350 muscles, Wheatley et al. [55] identified a mean hydraulic permeability value  
 351 of  $7.41 \cdot 10^{-11} \text{m}^2 \text{Pa}^{-1} \text{s}^{-1}$  with a standard error of  $2.2 \cdot 10^{-11} \text{m}^2 \text{Pa}^{-1} \text{s}^{-1}$ .  
 352 These values are higher than the calibrated values of this study (average  
 353  $(2.01 \pm 4.57) \cdot 10^{-13} \text{m}^2 \text{Pa}^{-1} \text{s}^{-1}$ , min:  $7.66 \cdot 10^{-15} \text{m}^2 \text{Pa}^{-1} \text{s}^{-1}$ ; max:  $2.40 \cdot 10^{-12}$   
 354  $\text{m}^2 \text{Pa}^{-1} \text{s}^{-1}$ ) but stay close in order of magnitude from the ones we found.  
 355 On the contrary, Gimmich et al. [27] reported a permeability to fluid flow  
 356  $\in [3.64 \cdot 10^{-14}; 1.27 \cdot 10^{-9}] \text{m}^2 \text{Pa}^{-1} \text{s}^{-1}$  if a dynamic viscosity of 1Pa.s is  
 357 considered.

358 A mean void ratio of  $0.56 \pm 0.3$  (min: 0.092; max: 0.94) was found in  
 359 this contribution. Argoubi and Shirazi-Adl [28] reported initial void ratios

360 between 0.1 and 0.3 for bones and cartilage. Our order of magnitude is  
361 higher but is still under an equivalent porosity of 50% for the muscle tissue.  
362 This is consistent also with the observation that skeletal muscle consists of  
363 approximately 75% bound and free fluid ( Sjogaard and Saltin [56]).

364 The calibrated results also showed some limitations of the poroelastic  
365 model used. Indeed, the toe-region of the curve did not follow the exper-  
366 imental curves as the initial slope is non-null. This could either be a con-  
367 sequence of the linear constitutive models used to represent the mechanical  
368 behaviour of both the solid scaffold (Hooke's law) and the fluids (Darcy's  
369 law) or come from experimental uncertainties (a default of parallelism be-  
370 tween the sample and the loading plate). In the second case, the interstitial  
371 fluid would first have a lower impact on the measured reaction force, and the  
372 toe region would change. This assumption is also supported by the results  
373 of Soltz and Ateshian [57] whose experimental stress curve of the cartilage  
374 with its interstitial fluid in confined compression also has a non-null initial  
375 slope.

376 Although the authors had access to the experimental unconfined com-  
377 pression data, the authors have not been able, in this work, to numerically  
378 reproduce, in a relevant way, the boundary conditions of the experiment.  
379 This is a limitation of the current work because demonstrating that the pro-  
380 posed model is capable of reproducing the mechanical response of skeletal  
381 muscle tissue under different loading and boundary conditions (i.e. Con-  
382 fined/Unconfined Compression, slow/fast loading conditions) would further  
383 establish that poro-elasticity is sufficient to capture the underlying phys-  
384 ical mechanisms that give rise to the time dependent stress-strain behaviour.  
385 Future work will focus on this aspect.

386 Despite the limitations of the present modelling work, this contribution  
387 provides an important step toward a mechanistic interpretation of passive  
388 muscle tissue undergoing compression in the context of **Deep Tissue Injury**  
389 prevention. Results support the idea that the extracellular fluid contributes  
390 to the apparent viscoelastic behaviour of passive muscle tissue under confined  
391 compression. One main limitation of this work is the lack of experimental  
392 evidences on the micro-structural organisation and composition of the sam-  
393 ples (porosity, permeability). This leads to the identification of constitutive  
394 parameters that are not unique and which affects the interpretation of the  
395 material mechanical behaviour. Further work will focus on experimental  
396 assessment of the impact of these assumptions and explore feasibility of de-  
397 veloping non-invasive methods to calibrate these parameters based on in vivo

398 data.

399 Building upon recent developments on cancer modelling (Urcun et al.  
400 [34], Sciumè et al. [35], Sciumè [36], Gray and Miller [37], Mascheroni et al.  
401 [38]), a potential perspective work is to couple the current modelling frame-  
402 work with multiphase/mutliphysics models of bio-chemical processes respon-  
403 sible of the onset of **Deep Tissue Injury** initiation, and to assess the impact of  
404 these parameters on the mechanical response. The interplay between chemi-  
405 cal-biological-mechanical factors is key to understand and eventually predict  
406 the initiation and propagation of soft tissue damage under extreme conditions  
407 of deformation and ischaemia. This kind of approach could be necessary in  
408 order to shed light on the relative importance (and the existence or absence of  
409 coupling according to the sub-populations at risk) of the parameters proven  
410 to be decisive in the development of pressure **ulcers**.

## 411 5. Conclusions

412 To test the hypothesis that poroelasticity is capable of reproducing the  
413 apparent viscoelastic behaviour of passive muscle tissue under confined com-  
414 pression, an axisymmetric Finite Element model was developed in ABAQUS.  
415 For each of the N=31 cylindrical porcine samples tested under fast and slow  
416 confined compression by Vaidya and collaborators, a one-to-one inverse anal-  
417 ysis was performed to calibrate the specimen-specific constitutive parameters.  
418 The peak stress and consolidation were recovered for most of the samples  
419 (N=25) by the poroelastic model. The strength of the proposed model of  
420 this study is its fewer number of variables. This contribution provides an  
421 important step toward a mechanistic interpretation of passive muscle tissue  
422 undergoing compression in the context of **Deep Tissue Injury** prevention.  
423 Poroelasticity also represents a promising approach for integrating multi-  
424 scale/multiphysics data to probe biologically relevant phenomena at a smaller  
425 scale. The incorporation of poroelasticity to clinical models of **Deep Tissue**  
426 **Injury** formation could lead to more precise and mechanistic explorations of  
427 soft tissue injury risk factors.

## 428 6. Declaration of competing interest

429 Authors have no conflicts of interest to report.

430 **7. Acknowledgment**

431     The authors received no financial support for the research, authorship,  
432 and/or publication of this article.

433 **Appendix A. Supplementary Data**

434 Supplementary data to this article (.inp ABAQUS files, pre and post  
435 processing python files for ABAQUS, calibrated and raw data) can be found  
436 online.

437 **Appendix B. Porous medium mechanics**

438 Considering its architecture, the passive muscle tissue can be considered  
439 as a multi-phase tissue, composed by a solid scaffold and two liquid phases:  
440 the blood contained by blood vessels and the surrounding Interstitial Fluid  
441 (IF) (Sciumè [36]). With experimentation performed *ex vivo* on small sam-  
442 ples, it was assumed that there was no blood and the model was based only  
443 on a single level of porosity with the solid scaffold, filled with IF. Also, the  
444 porous medium was assumed to be fully saturated.

445 In the remainder of the test, the following convention is assumed:  $\bullet^s$   
446 denotes the solid phase and  $\bullet^l$  denotes the fluid phase (IF). The primary  
447 variables of the problem are the pressure applied in the pores of the porous  
448 medium and the displacement of the solid scaffold. Then, a first relationship  
449 (eq. B.1) linking the different volume fractions, can be defined. The volume  
450 fraction of the phase  $\alpha$  is defined by (eq. B.2).  $\varepsilon^l$  is also called the porosity  
451 of the medium and is related to the void ratio,  $e$ , by eq. B.3.

$$\varepsilon^s + \varepsilon^l = 1 \quad (\text{B.1})$$

$$\varepsilon^\alpha = \frac{\text{Volume}^\alpha}{\text{Volume}^{total}} \quad (\text{B.2})$$

$$e = \frac{\varepsilon^l}{1 - \varepsilon^l} \quad (\text{B.3})$$

452 Assuming that there is no inter-phase mass transport, the spatial form of  
453 the mass balance equation of the solid and liquid phase is respectively then  
454 given by equations (eq. B.4) and (eq. B.5).

$$\frac{D^s}{Dt}(\rho^s \varepsilon^s) + \rho^s \varepsilon^s \nabla \cdot \mathbf{v}^s = 0 \quad (\text{B.4})$$

$$\frac{D^s}{Dt}(\rho^l \varepsilon^l) + \nabla \cdot (\rho^l \varepsilon^l (\mathbf{v}^l - \mathbf{v}^s)) + \rho^l \varepsilon^l \nabla \cdot \mathbf{v}^s = 0 \quad (\text{B.5})$$

455 Where  $\frac{D^s}{Dt}$  is the particle derivative with respect to the movement of the phase  
 456  $\bullet^s$ ,  $\mathbf{v}^\alpha$  is the local velocity vector of the phase  $\alpha$  and  $\rho^\alpha$  the density of the  
 457 phase  $\alpha$ .

458 Using (eq. B.1), (eq. B.4) gives:

$$\frac{D^s}{Dt}(\rho^s(1 - \varepsilon^l)) + \rho^s(1 - \varepsilon^l)\nabla \cdot \mathbf{v}^s = 0 \quad (\text{B.6})$$

459 For the fluid phase, Darcy's law (eq. B.7) is used to evaluate the fluid  
 460 flow in the porous medium.

$$\varepsilon^l(\mathbf{v}^l - \mathbf{v}^s) = -\frac{k^\varepsilon}{\mu^l}(\nabla p - \rho^l \mathbf{g}) \quad (\text{B.7})$$

461 Where  $k^\varepsilon$  is the intrinsic permeability ( $\text{m}^2$ ),  $\mu^l$  is the dynamic viscosity (Pa.s),  
 462  $p$  the pressure and  $\mathbf{g}$  the gravity.  $\frac{k^\varepsilon}{\mu^l}$  is called the hydraulic permeability.

463 Then, (eq. B.7) is injected in (eq. B.5) as follows:

$$\frac{D^s}{Dt}(\rho^l \varepsilon^l) - \nabla \cdot (\rho^l (\frac{k^\varepsilon}{\mu^l} (\nabla p - \rho^l \mathbf{g}))) + \rho^l \varepsilon^l \nabla \cdot \mathbf{v}^s = 0 \quad (\text{B.8})$$

$$\iff \frac{D^s}{Dt}(\rho^l \varepsilon^l) - \nabla \cdot \rho^l (\nabla (\frac{k^\varepsilon}{\mu^l} p)) + \nabla \cdot (\rho^l \frac{k^\varepsilon}{\mu^l} \mathbf{g}) + \rho^l \varepsilon^l \nabla \cdot \mathbf{v}^s = 0 \quad (\text{B.9})$$

464 Concerning the mechanical constitutive model, similarly to what was pro-  
 465 posed by Terzaghi for a 1D consolidation (Appendix C.1), an effective stress  
 466 tensor denoted  $\mathbf{t}^{eff}$  is responsible for all deformation of the solid ECM scaf-  
 467 fold. Hence the total stress tensor is defined by (eq. B.10).

$$\mathbf{t}^{tot} = \mathbf{t}^{eff} - \beta p \mathbf{I}_d \quad (\text{B.10})$$

468 Where  $\beta$  is the Biot's coefficient and  $\mathbf{I}_d$  is the identity matrix.

469 Assuming linear elastic behaviour, the effective stress tensor is defined by  
 470 (eq. B.11).

$$\mathbf{t}^{eff} = \mathbf{C} : \mathbf{d} \quad (\text{B.11})$$

471 Then, applying the conservation of momentum, the governing equations  
 472 of this one level porous medium are:

$$\frac{D^s}{Dt}(\rho^s(1 - \varepsilon^l)) + \rho^s(1 - \varepsilon^l)\nabla \cdot \mathbf{v}^s = 0 \quad (\text{B.12})$$

$$\frac{D^s}{Dt}(\rho^l \varepsilon^l) - \nabla \cdot \rho^l (\nabla (\frac{k^\varepsilon}{\mu^l} \mathbf{p})) + \nabla \cdot (\rho^l \frac{k^\varepsilon}{\mu^l} \mathbf{g}) + \rho^l \varepsilon^l \nabla \cdot \mathbf{v}^s = 0 \quad (\text{B.13})$$

$$\nabla \cdot (\mathbf{t}^{tot}) + f_v = \rho^s \gamma^s \quad (\text{B.14})$$

473 Where  $f_v$  are the force densities applied to the medium and  $\gamma^s$  is the acceleration of the  
 474 solid phase.

475 Three boundaries were defined: the first one,  $\Omega_u$  has imposed displace-  
 476 ment (eq. B.15), the second one  $\Omega_s$  has imposed external forces (eq. B.16)  
 477 and  $\Omega_p$  is submitted to an imposed pressure (fluid leakage condition (eq.  
 478 B.17)). We obtain:

$$\mathbf{t}^{eff} = \mathbf{t}^{imposed} \text{ on } \Omega_s \quad (\text{B.15})$$

$$\mathbf{u}^s = \mathbf{u}^{imposed} \text{ on } \Omega_u \quad (\text{B.16})$$

$$p = 0 \text{ on } \Omega_p \quad (\text{B.17})$$

### 479 Appendix C. Poroelasticity to capture the time-dependent response 480 of muscle

481 Most of biological soft tissues has a porous/fibrous nature consisting of a  
 482 solid scaffold giving mechanical stability and one or more fluid or pseudo-fluid  
 483 phases which saturate the porosity. Hence, to mechanistically model a bio-  
 484 logical human (or animal) tissue accounting for the interaction between the  
 485 solid matrix (primarily constituted by proteins and collagen fibers) and the  
 486 fluid phases one must use porous media mechanics. Despite this conscious-  
 487 ness, researchers are still today much more used to employ viscoelasticity to  
 488 model the time-dependent behavior of soft tissues. If on one hand its is true  
 489 that viscoelastic models are typically very effective to fit usual experimental  
 490 tests, however the underlying physical mechanisms that give rise to the time-  
 491 stress dependent behavior is not well known and found material parameters  
 492 may vary with the considered boundary conditions.

493 Lets we consider two reference models: i) a two-phase (one solid-one fluid)  
 494 poroelastic model and ii) a rheological viscoelastic model constituted by a

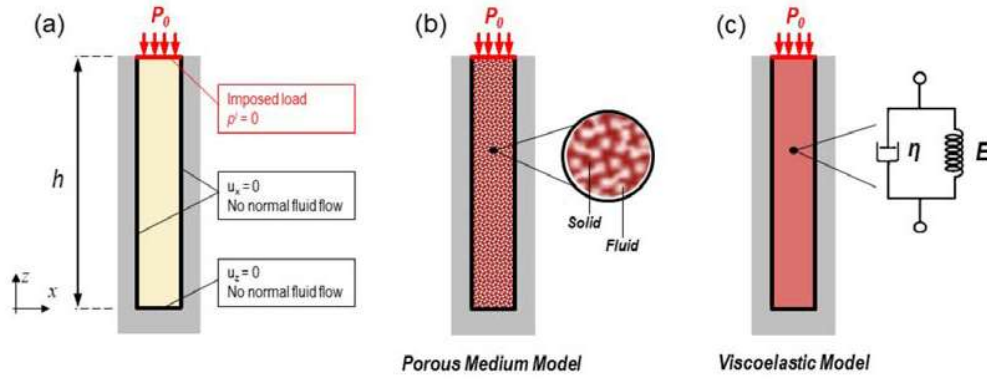


Figure C.5: One dimensional consolidation. (a) Geometry and boundary conditions; (b-c) porous medium and viscoelastic models

495 Kelvin-Voight chain; and use these two models to simulate a 1D confined  
 496 compression test. In this test the tissue is constrained in a cylindrical or  
 497 prismatic chamber and compressed at the top surface with a constant pres-  
 498 sure,  $p_0$ . The specimen is fully sealed with the exception of the top surface  
 499 where a porous membrane allows drainage of the inside fluid during the test.  
 500 The geometry and boundary conditions of the test are represented in Figure  
 501 C.5. This kind of test, which takes up the paradigms of one of the most im-  
 502 portant characterization essay in soil mechanics (it is named oedometer test  
 503 or 1D consolidation test), is a very frequent test performed to characterize  
 504 the dynamics response of biological soft tissue.

#### 505 *Appendix C.1. Terzaghi's analytic solution*

506 The Terzaghi analytical solution given by (eq. C.1) gives the solution  
 507 to 1D porous medium mechanics a series expansion function of the 1D-  
 508 coordinate. Hereunder are recalled the hypotheses of the Terzaghi's solu-  
 509 tion (Tavenas, F. et al. [58]):

- 510 1. the sample is submitted to small and unidirectional strains
- 511 2. The solid grains and fluid are supposed in-compressible
- 512 3. The material is homogeneous
- 513 4. The mechanical parameters stay constant during all the settlement
- 514 5. The fluid leakage is unidirectional and follows the Darcy's law



- 515 6. There is a linear law between the effective stresses and volume variation  
516 of the soil  
517 7. The soil has no structural viscosity or secondary settlement

$$p = \frac{4p_0}{\pi} \sum_{k=1}^{+\infty} \frac{(-1)^{k-1}}{2k-1} \cos\left[(2k-1)\frac{\pi}{2}\frac{z}{h}\right] \exp\left[-(2k-1)^2 \frac{\pi^2}{4} \frac{c_v t}{h^2}\right] \quad (\text{C.1})$$

$$c_v = \frac{k^\varepsilon}{\mu^l \left(S + \frac{\beta^2}{M}\right)} \quad (\text{C.2})$$

$$M = \frac{3K^s(1-\nu)}{(1+\nu)} \quad (\text{C.3})$$

$$S = \frac{\beta - \varepsilon_0^l}{K^s} + \frac{\varepsilon_0^l}{K^l} \quad (\text{C.4})$$

518 Where  $p_0$  is the full applied load,  $z$  is the altitude,  $h$  is the initial height of the sample ,  
519  $c_v$  is the consolidation coefficient defined by (eq. C.2),  $M$  the longitudinal modulus (eq.  
520 C.3),  $K^\alpha$  the bulk's modulus of the  $\alpha$  phase,  $\nu$  the Poisson's ratio,  $S$  the inverse of the  
521 Biot Modulus (eq. C.4),  $\beta$  is the Biot coefficient and  $\varepsilon_0^l$  is the initial porosity.

522 Looking to (eq. C.1), a consolidation time  $T_v = \frac{h^2}{c_v}$  was defined. Ususally,  
523 in the assumption of a compressibility of the phases larger than the porous  
524 medium compressibility, then  $\beta = 1$  and  $S = 0$  gives:

$$c_v = \frac{k^\varepsilon M}{\mu^l} \quad (\text{C.5})$$

$$T_v = \frac{h^2 \mu^l}{k^\varepsilon M} \quad (\text{C.6})$$

525 The consolidated stress,  $t^{\text{consolidated}}$  was also computable (eq. C.7),

$$t^{\text{consolidated}} = M \frac{u_{\text{imposed}}}{h} \quad (\text{C.7})$$

526 Where  $u_{\text{imposed}}$  is the imposed displacement on the top surface and  $h$  is the initial height  
527 of the sample.

528 So in this minimal version of porous medium model the behaviour is gov-  
529 erned by three parameters: the elastic coefficients  $E$  and  $\nu$  (which determine

530  $M$ ) and the ratio between the intrinsic permeability of the solid and the dy-  
 531 namic viscosity of the fluid  $\frac{k}{\mu^l}$ . From eq. C.1 quasi-analytical solutions can  
 532 be derived for the vertical strain and vertical displacement along the vertical  
 533 coordinate.

534 *Appendix C.2. Viscoelastic formulation*

535 The analytical solution of the viscoelastic model has a much simpler form  
 536 and gives the vertical displacement of the points along the vertical coordinate  
 537 of the column as a function of time

$$u_z(z, t) = -\frac{p_0 t}{M} \left[ 1 - \frac{E t}{\eta} \right] \quad (\text{C.8})$$

538 So also in this model the behaviour is governed by three parameters: the  
 539 elastic coefficients  $E$  (stiffness of the spring in the 1D rheological model) and  
 540  $\nu$  and the viscosity of the damper  $\eta$ .

541 *Appendix C.3. Comparison between the two solutions*

542 For the simulated experiment the column height,  $h$  is of 1 cm and the  
 543 pressure,  $p_0$ , imposed at the top of the column is equal to 10 Pa. For the  
 544 porous medium formulation the following parameters are assumed: Young's  
 545 modulus  $E$  equal to 1 kPa; Poisson's ration  $\nu$  equal to 0.4; intrinsic perme-  
 546 ability of the solid scaffold,  $k$ , equal to  $4 \times 10^{-16}$  m<sup>2</sup>; and dynamic viscosity  
 547 of the fluid,  $\mu^l$ , equal to 0.001 Pa.s. For the viscoelastic model the Young's  
 548 modulus and the Poisson's ratio have the same values of the porous medium  
 549 model. For the viscosity of the damper,  $\eta$ , a value of  $4.4 \times 10^7$  Pa.s has been  
 550 identified which, for  $h$  equal to 1 cm, gives an overall response in term of ver-  
 551 tical displacement of the top point very similar to that of the porous medium  
 552 model (see Figure C.6.d solid lines). In this figure we can observe that the  
 553 initial agreement between the two formulations is not optimal; however, after  
 554 24 hours the two curves are superposed. To better understand the behaviour  
 555 of the two models we can analyse more in depth such results by plotting the  
 556 vertical displacement along the vertical coordinate at different times for the  
 557 porous medium and the viscoelastic models. In Figure C.6.c we can observe  
 558 that in the porous medium model the displacement in proximity of the drying  
 559 surface grows initially more rapidly than in the viscoelastic case since this  
 560 area is rapidly consolidated in the first phase of the compression process.  
 561 This can be more easily understood looking at Figure C.6.b which shows the  
 562 fluid pressure along the vertical coordinate at different times for the porous

563 medium model. We can observe that the pressure decreases progressively  
 564 over the time due to the consolidation process.

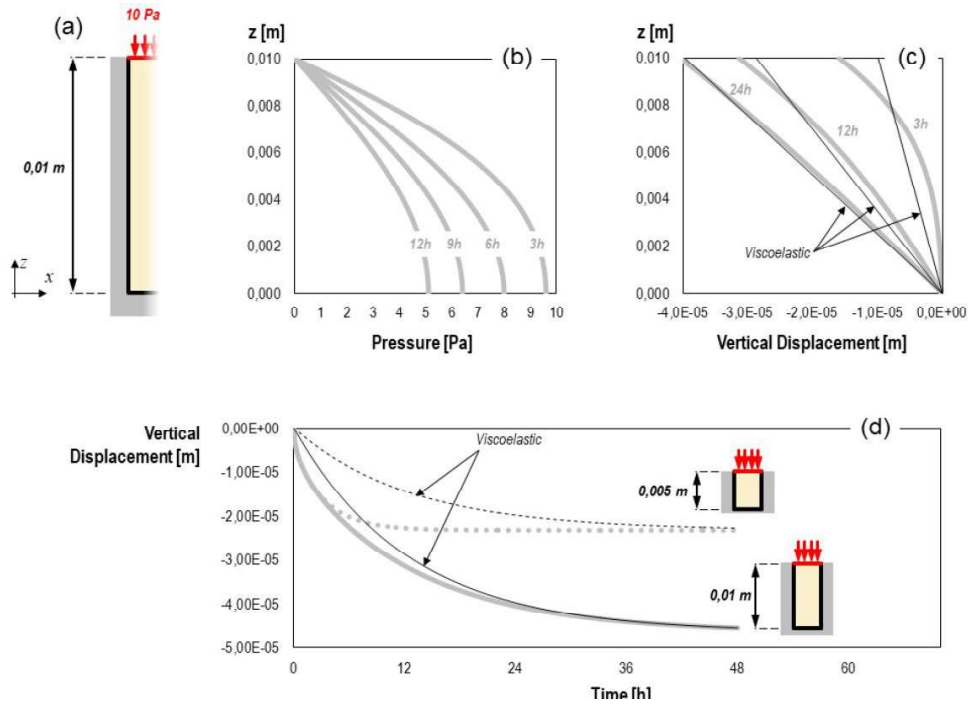


Figure C.6: Results for the 1D consolidation case. (a) Specimen geometry. (b) Fluid pressure along the vertical coordinate at different times (porous medium model). (c) Vertical displacement along the vertical coordinate at different times for the porous medium model (gray line) and the viscoelastic model (black line). (d) Vertical displacement of the top surface versus time for the porous medium model (gray line) and the viscoelastic model (black line); two cases are considered:  $h = 1$  cm (solid lines) and  $h = 0.5$  cm (dashed lines).

565 Hence, this initial heterogeneity of strain along the vertical coordinated  
 566 cannot be reproduced with the viscoelastic model since the drainage of the  
 567 fluid is not explicitly modelled. However, the worst is still to come. Let's  
 568 we consider now a column with  $h$  equal to 0.5 cm, one half of the previ-  
 569 ously assumed height. The overall vertical displacement of the top surface  
 570 is depicted in Figure C.6.d. for the porous medium (gray dashed line) and  
 571 viscoelastic (black dashed line) models. The figure shows that this time the  
 572 dynamics is fully different. In the porous medium case the column consoli-  
 573 dates much faster than in the viscoelastic case. If we compare the solution

574 of  $h = 0.5$  cm (dashed lines) with those of  $h = 1$  cm (solid lines) we see that  
575 the dynamics of the viscoelastic model remains the same (obviously with a  
576 different asymptotic tendency) while the porous medium model consolidates  
577 almost four time faster for  $h = 0.5$  cm. To decipher the reason of the discor-  
578 dance between solutions of the viscoelastic and porous medium models one  
579 can consider the unit of the factors that drive time dependent response in the  
580 two cases. Looking firstly at the analytical solution of the viscoelastic model  
581 from eq. C.8 we deduce that the characteristic time of the consolidation  
582 process is proportional to  $\frac{\eta}{E}$  (that quantity has the dimension of a time).  
583 In the porous medium model the time dependent response is governed by  
584 the consolidation coefficient and the characteristic time of the consolidation  
585 process is proportional to  $\frac{h^2}{c_v}$  (eq. C.6) and that therefore the length of the  
586 drainage path  $h$  has a capital impact on the consolidation dynamics. From  
587 these analyses we deduce that for the porous medium model once parame-  
588 ter are identified these remain suitable also in other experimental situations.  
589 Conversely, if we want to mimic the behaviour of a porous material with a  
590 viscoelastic model we must adjust the parameter  $\eta$  accounting for the spec-  
591 imen size and boundary conditions. If on one hand this is feasible for a 1D  
592 case, on the other hand we can imagine that could be very difficult for more  
593 complex configurations.

#### 594 Appendix D. Terzaghi's analytic solution with Abaqus

595 For the confined compression tests, the expected result was similar to a  
596 1D compression. Hence, the Terzaghi analytical solution given by (eq. C.1)  
597 was used to assess the reliability of the ABAQUS model considered. The  
598 analytical solution is recalled section Appendix C.1.

Solid Phase			Fluid Phase			
Linear Elastic Law		Soil Grain Bulk Modulus	Darcy's Law			Fluid Bulk Modulus
E (kPa)	$\nu$ (-)	$K^s$ (MPa)	$k$ ( $\text{m}^2 \text{Pa}^{-1} \text{s}^{-1}$ )	Dynamic Viscosity (Pa s)	Void ratio (-)	$K^t$ (MPa)
1.0	0.4	0.001 (full line) / 2200 (dashed line)	$4 \cdot 10^{-13}$	1.0	1.0	2200

Table D.4: Parameters used in the verification model

599 According to section 2.2, a preliminary study was carried out over a small  
600 strain model. A 2D axi-symmetric ABAQUS model composed of (n=60  
601 CAX4PH elements) of an imposed load experiment was proposed. An im-  
602 posed pressure of 10 Pa was applied on the top surface and boundary con-  
603 ditions are presented Figure C.5. The material parameters are given Table  
604 D.4. Two different conditions were tested:  $K^s = 0.001\text{MPa} \implies \beta =$

605  $1 - \frac{E}{3K^s(1-2\nu)} = 0.83$  which is lower than the soil bulk modulus expected for  
 606 the muscle and  $K^s = 2.2e9\text{MPa} \implies \beta = 1 - \frac{E}{3K^s(1-2\nu)} \approx 1.0$  which allowed  
 607 to be closer to the assumption 2 above.

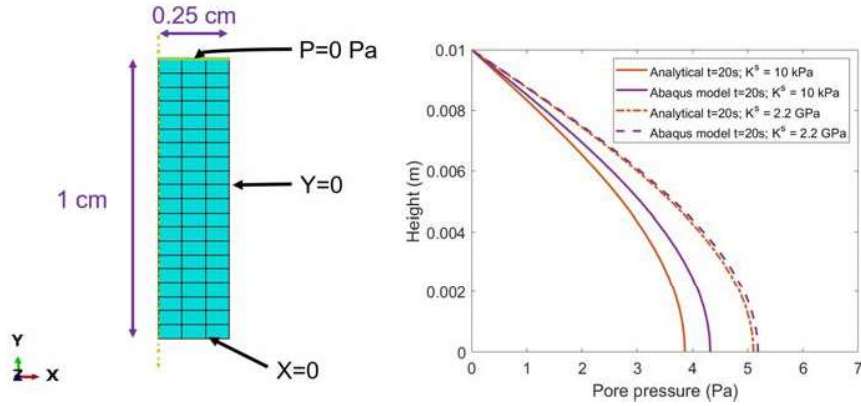


Figure D.7: Discretized Finite Element model (left) and comparison to the analytical solution (right)

608 The result obtained are presented on the right of Figure D.7. The dashed  
 609 curves correspond to the quasi-incompressible soil grains and plain curves to  
 610 the non-incompressible soil grain model. As expected, the quasi-incompressible  
 611 soil grains' curve was quasi-super-imposed. There was a difference for the  
 612 non-incompressible soil grain, probably because the hypotheses were not fully  
 613 covered but the order of magnitude was good.

614 Finally, as our samples were submitted to high strains, the use of the anal-  
 615 itycal solution was not possible to directly model the available experimental  
 616 data.

## 617 Appendix E. Hyper-elasticity models for the buttock tissue

618 To quantitatively assess the influence of the assumed constitutive law  
 619 when simulating the finite deformation of soft tissue in compression in the  
 620 context of Pressure Ulcer prevention, a the semi-confined compression exper-  
 621 iment is simulated (Figure E.8 below). The numerical experiment consists in  
 622 testing in compression a cylindrical specimen with low-aspect ratio. In the  
 623 semi-confined configuration, the top and bottom faces of the specimen are  
 624 rigidly attached to the platens of the stress-strain machine to ensure no-slip  
 625 boundary conditions.

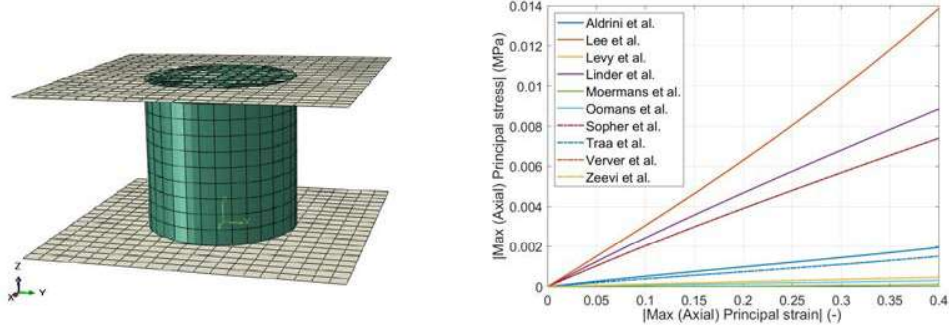


Figure E.8: Numerical model of the semi-confined experiment proposed (left) and resulting stress-strain curves (right). The references of the legend correspond to the ones of Table E.5

626 The constitutive laws found in the litterature are mostly variation around  
627 three main strain-energy density functions : Ogden Law (E.1), Mooney-  
628 Rivlin and Neo-Hookean (E.3). The Mooney-Rivlin is computed in abaqus  
629 as a generalized Rivlin model with one mode (E.2). For each equation,  $W$  is  
630 the strain energy density function,  $\bar{\lambda}_i$  are the deviatoric stretches,  $\bar{I}_i$  are the  
631 deviatoric invariants of the Green-Cauchy left transformation tensor and  $J$   
632 the Jacobian of the transformation tensor.

$$W(\bar{\lambda}_i) = \frac{\mu_1}{\alpha_1} \left( \sum_i \bar{\lambda}_i^{\alpha_1} - 3 \right) + \frac{1}{D_1} (J - 1)^2 \quad (\text{E.1})$$

$$W(\bar{I}_i) = C_{10}(\bar{I}_1 - 3) + C_{01}(\bar{I}_2 - 3) + \frac{1}{D_1} (J - 1)^2 \quad (\text{E.2})$$

$$W(\bar{I}_i) = C_{10}(\bar{I}_1 - 3) + \frac{1}{D_1} (J - 1)^2 \quad (\text{E.3})$$

633 Some articles used different forms of those equations but due to the as-  
634 sumption of incompressibility, all those writings are equivalent. We computed  
635 the equivalent parameters to be used in ABAQUS. The table E.5 presents  
636 for each article the considered constitutive law and the parameters used in  
637 ABAQUS. As ABAQUS uses pre-encoded equation, the parameters or the  
638 equation formulation can be simplified or slightly modified in regard of the  
639 one used in the articles.

640 Looking to Figure E.8, the hyper-elastic laws with their associated pa-  
641 rameters for muscle tissue may be, at least during the 15 first percent of

642 compression, approximated by a linear-elastic law for the solid scaffold.

643 **Appendix F. Poroelastic model parameter identification assuming**  
 644 **a highly compressible drained solid phase (Poisson’s**  
 645 **ratio of 0.2)**

646 *Appendix F.1. Calibration of the average experimental relaxation curve*

647 Similarly to the previous section, the result of the calibration of the av-  
 648 erage relaxation stress-time curve is superimposed in Figure F.9 onto the  
 649 average experimental sample stress-time curve and the experimental corri-  
 650 dor. The calibrated visco-hyper-elastic numerical model reported in Vaidya  
 651 and Wheatley [39] is also superimposed for the ease of comparison.

652 The parameters identified were, respectively, for fast and slow strain-  
 653 rate: Young’s modulus of 149 kPa, Poisson’s ratio of 0.2, void ratio  $e$  of  
 654 1.0 (which corresponds to a porosity of 50%) and hydraulic permeability of  
 655  $k = 2.32 \cdot 10^{-14} \text{ m}^2 \text{ Pa}^{-1} \text{ s}^{-1}$ ; Young’s modulus of 99.3 kPa, Poisson’s ratio  
 656 of 0.2, void ratio  $e$  of 0.72 (which corresponds to a porosity of 42%) and  
 657 hydraulic permeability of  $k = 4.16 \cdot 10^{-14} \text{ m}^2 \text{ Pa}^{-1} \text{ s}^{-1}$ .

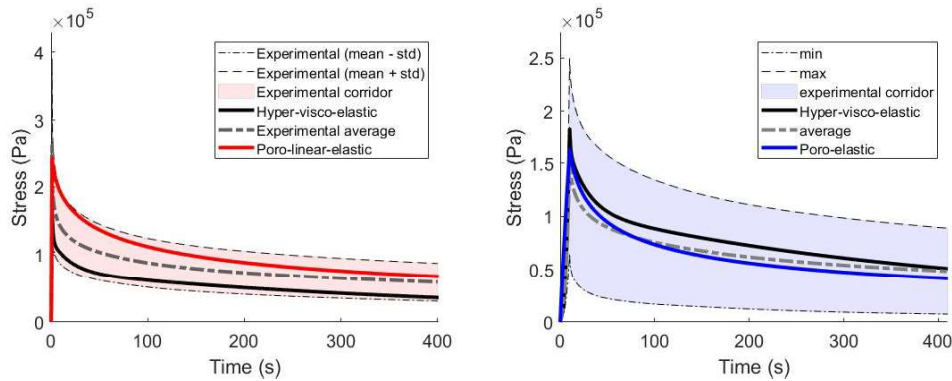


Figure F.9: Results for the fast strain-rate (left) and for the slow strain-rate (right) average experimental relaxation curve calibration. The experimental corridor of the campaign of Vaidya and Wheatley [39] is light red for the fast strain rate and light blue for the slow one, the average experimental stress is in dashed grey. The visco-hyper-elastic model calibrated in Vaidya and Wheatley [39] is in black while poroelastic model predictions with a Poisson’s ratio of 0.2 are in red for the fast strain rate and blue for the slow strain-rate.

658 Quantitative error metrics of the optimisation procedure for the proposed  
 659 poro-linear-elastic model are reported in Table F.6. The different components

660 of the cost function are the same than section 3. These metrics were also  
661 assessed on the numerical curves stress-time curve fitted with the visco-hyper-  
662 elastic model in Vaidya and Wheatley [39] and reported in the table for  
663 the sake comparison. The cost function between the optimised poroelastic  
664 numerical curve and the experimental curve is smaller with the proposed  
665 poroelastic model than with the visco-hyper-elastic model in Vaidya and  
666 Wheatley [39] (0.0022 versus 0.21 for the slow and 0.0375 versus 0.2477 for  
667 the fast).

668 *Appendix F.1.1. One to one sample calibration*

669 The one to one calibration was carried out on the n=16 samples for fast  
670 strain-rate and n=15 samples for slow strain-rate. The corresponding stress-  
671 time curves for each sample are reported in Figures F.10 and F.11 respectively  
672 for the slow and for the fast loading rates. Looking to the 31 calibrated  
673 curves, the slope between 350 s and 400 s is mostly approximated: most of  
674 the samples are not fully consolidated at the end time of the experiments  
675 as the slope is non-null. Also the peak stress is mostly recovered by the  
676 poroelastic model.



Article	Constitutive Law	ABAQUS Parameters
Al-Dirini et al. [22]	Ogden	$\mu_1 = 1.91e - 3\text{MPa}$ $\alpha_1 = 4.6$ $D_1 = 9.179\text{MPa}^{-1}$
Lee et al. [46]	Moonley-Rivlin	$C_{01} = 1.65e - 3\text{MPa}$ $C_{10} = 3.35e - 3\text{MPa}$ $D_1 = 4.03\text{MPa}^{-1}$
Levy et al. [48]	Neo-Hookean	$D_1 = 2.83\text{MPa}^{-1}$ $C_{10} = 3.55e - 3\text{MPa}$
Linder-Ganz et al. [11]	Neo-Hookean	$D_1 = 1.18\text{MPa}^{-1}$ $C_{10} = 4.25e - 3\text{MPa}$
Moerman et al. [14]	Ogden	$\mu_1 = 5.575e - 4\text{MPa}$ $\alpha_1 = 12$ $D_1 = 7.47\text{MPa}^{-1}$
Oomens et al. [44]	Ogden	$\mu_1 = 3.0e - 4\text{MPa}$ $\alpha_1 = 5$ $D_1 = 13.36\text{MPa}^{-1}$
Sopher et al. [49]	Neo-Hookean	$D_1 = 2.817\text{MPa}^{-1}$ $C_{10} = 3.55e - 3\text{MPa}$
Traa et al. [45]	Ogden	$\mu_1 = 1.49e - 3\text{MPa}$ $\alpha_1 = 5$ $D_1 = 57\text{MPa}^{-1}$
Verver et al. [47]	Moonley-Rivlin	$C_{01} = 1.65e - 3\text{MPa}$ $C_{10} = 3.35e - 3\text{MPa}$ $D_1 = 5.04\text{MPa}^{-1}$
Zeevi et al. [50]	Neo-Hookean	$D_1 = 53.3\text{MPa}^{-1}$ $C_{10} = 2.25e - 3\text{MPa}$

Table E.5: Table gathering all the considered articles and their associated parameters used in ABAQUS

Model	Strain-rate	$J_1$ (eq. 3)	$J_2$ (eq. 4)	$J_3$ (eq. 5)	$J$ (eq. 6)
Uncoupled Yeoh/Prony visco-hyper-elastic	Slow	0.0283	0.5936	0.0081	0.21
	Fast	0.1559	0.4611	0.0046	0.2477
Poro-linear-elastic Current study	Slow	0.0014	0.00055	0.0046	0.0022
	Fast	0.0056	0.0974	0.0093	0.0375

Table F.6: Error metrics of the average experimental stress calibrated models for the fast and slow strain-rates of the model proposed by Vaidya and Wheatley [39] and the current study's model

Solid Phase		Fluid Phase		Error Metrics				
Linear Elastic Law		Darcy's Law		Total	Peak Stress	Slope	RMS	
E (kPa)	$\nu$ (-)	Soil Grain Bulk Modulus $K^s$ (MPa)	Darcy's Law $k$ ( $m^2 Pa^{-1} s^{-1}$ )	Fluid Bulk Modulus $K^f$ (MPa)	$J$ (eq. 6)	$J_1$ (eq. 3)	$J_2$ (eq. 4)	$J_3$ (eq. 5)
$116.02 \pm 31.89$	0.2	0.799	$1.16 \cdot 10^{-12} \pm 1.93 \cdot 10^{-12}$	2200	$0.121 \pm 0.161$	$0.0167 \pm 0.0228$	$0.322 \pm 0.472$	$0.024 \pm 0.022$
$133.75 \pm 24.54$	0.2	0.799	$1.87 \cdot 10^{-12} \pm 4.17 \cdot 10^{-12}$	2200	$0.12 \pm 0.13$	$0.069 \pm 0.086$	$0.422 \pm 0.269$	$0.016 \pm 0.0105$

Table F.7: Calibrated parameters and error metrics: mean and standard deviation. First line corresponds to slow-rate parameters and second line to fast-rate results

677 Table F.7 provides the mean and standard deviation of the calibrated  
678 parameters. The same order of magnitude is obtained whether the strain-  
679 rate was fast or slow. The measured error metrics of the calibration were  
680 respectively  $0.12 \pm 0.13$  and  $0.121 \pm 0.161$  (mean and standard deviation of  
681 all error metrics are provided Table F.7). Once again, these results support  
682 the apparent capacity of the model to mostly capture the peak stress and  
683 relaxation described previously also minimising the root mean square error  
684 metric.

685 To quantify the goodness of fit, the value of the cost function value at  
686 the solution  $\mathbf{J}_{final}^{tot}$  is given for each sample in figure F.12 below.

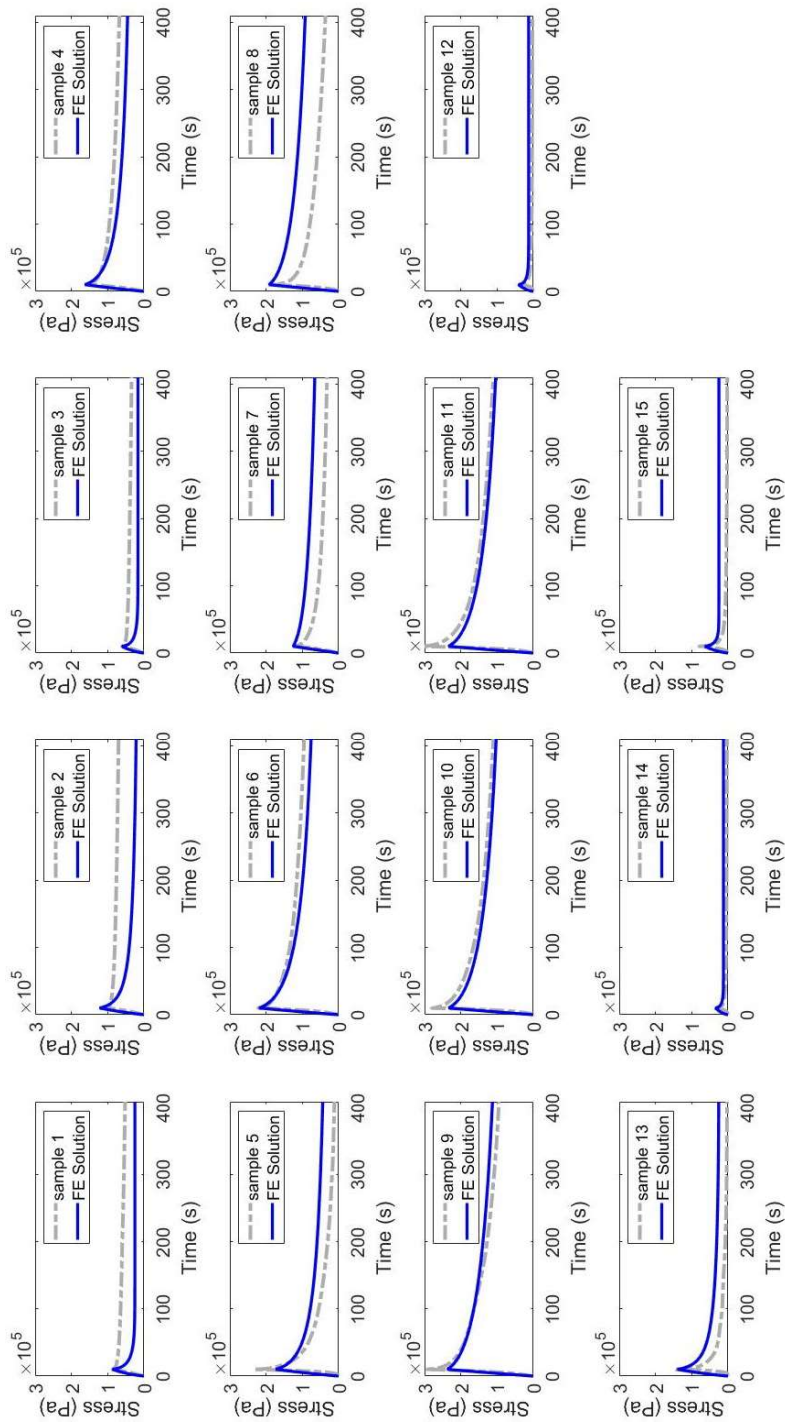


Figure F.10: All 15 FE samples calibrated models (blue) superimposed with the corresponding experimental data (light grey) for slow rate experiment

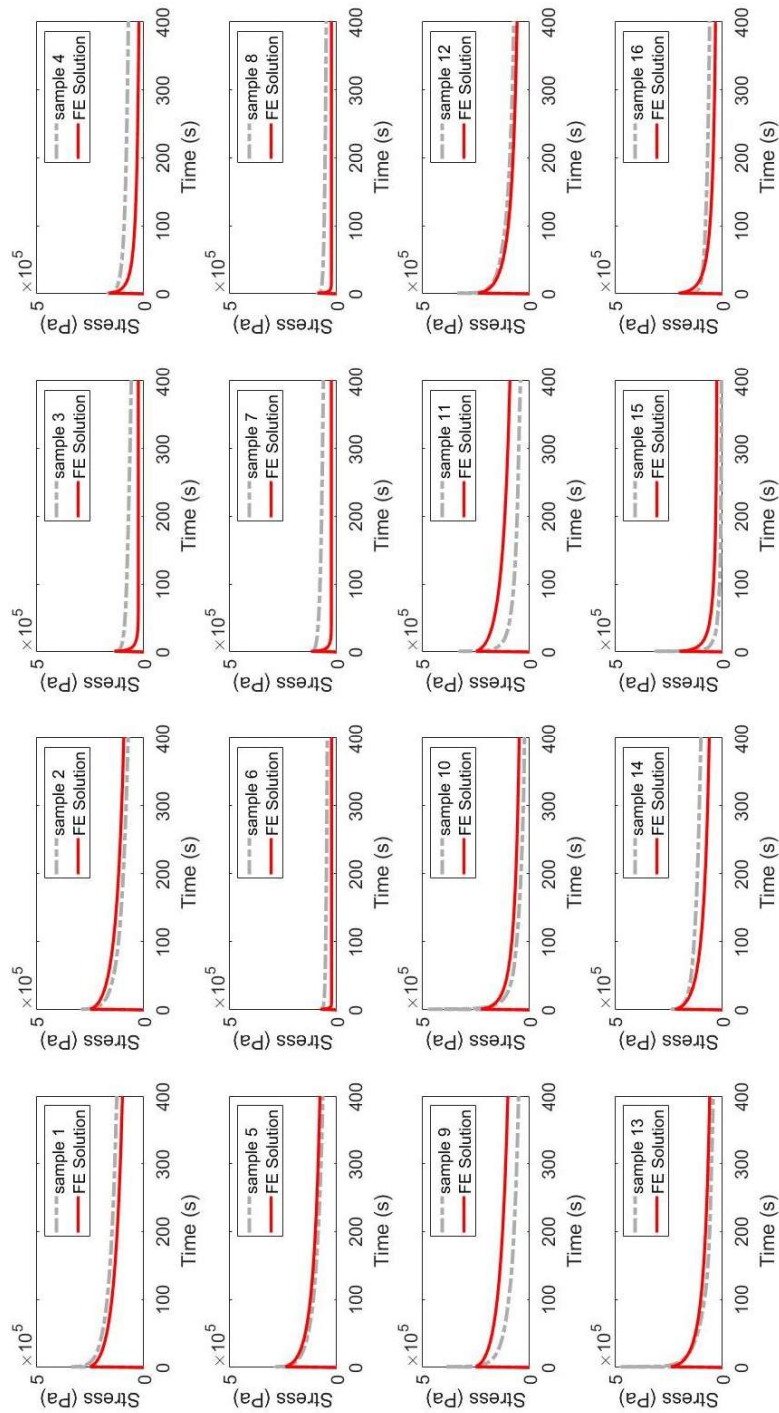


Figure F.11: All 16 samples FE calibrated models (red) superimposed with the corresponding experimental data (light grey) for fast rate experiment

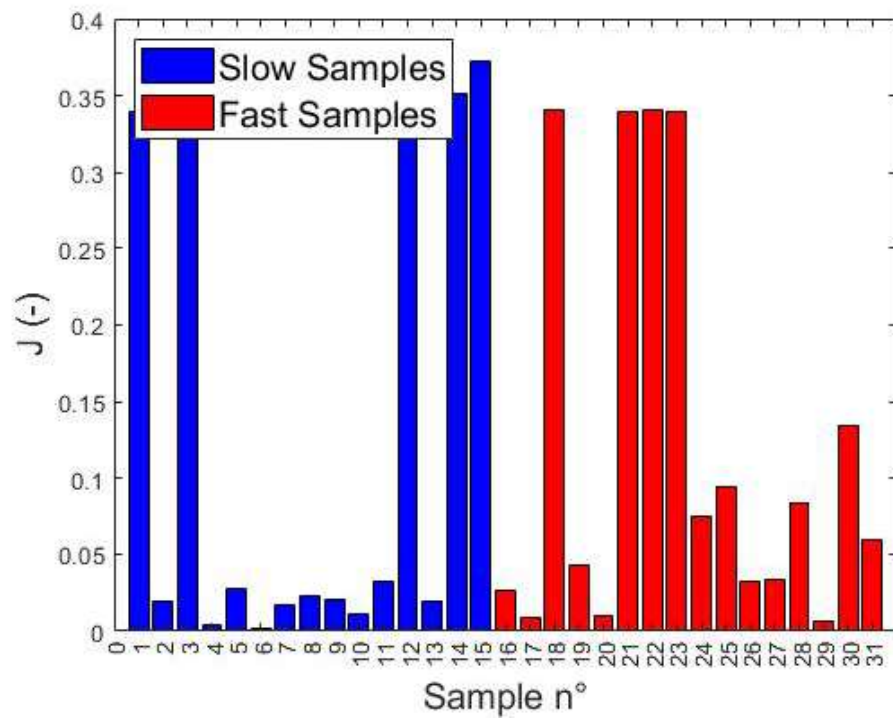


Figure F.12: Cost function value at the solution for each sample. Blue corresponds to samples tested with a slow strain-rate loading and red to the samples tested with fast strain-rate loading.

687 **References**

688 [1] A. Gefen, D. M. Brienza, J. Cuddigan, E. Haesler, J. Kottner,  
689 Our contemporary understanding of the aetiology of pressure ul-  
690 cers/pressure injuries, *International Wound Journal* n/a (2021). URL:  
691 <https://onlinelibrary.wiley.com/doi/abs/10.1111/iwj.13667>.  
692 doi:<https://doi.org/10.1111/iwj.13667>.

693 [2] A. Gefen, P. Alves, G. Ciprandi, F. Coyer, C. T. Milne, K. Ousey,  
694 N. Ohura, N. Waters, P. Worsley, J. Black, M. Barakat-Johnson,  
695 D. Beeckman, J. Fletcher, H. Kirkland-Kyhn, N. A. Lahmann,  
696 Z. Moore, Y. Payan, A.-B. Schlüer, Device-related pressure ul-  
697 cers: SECURE prevention, *Journal of Wound Care* 29 (2020)  
698 S1–S52. URL: <https://doi.org/10.12968/jowc.2020.29.sup2a.s1>.  
699 doi:10.12968/jowc.2020.29.sup2a.s1.

700 [3] G. Bennett, C. Dealey, J. Posnett, The cost of pres-  
701 sure ulcers in the UK, *Age and Ageing* 33 (2004)  
702 230–235. URL: <https://doi.org/10.1093/ageing/afh086>.  
703 doi:10.1093/ageing/afh086. arXiv:<https://academic.oup.com/ageing/article-pdf/33/3/>

704 [4] K. Ceelen, A. Stekelenburg, S. Loerakker, G. Strijk-  
705 ers, D. Bader, K. Nicolay, F. Baaijens, C. Oomens,  
706 Compression-induced damage and internal tissue strains are  
707 related, *Journal of Biomechanics* 41 (2008) 3399–3404.  
708 URL: <https://doi.org/10.1016/j.jbiomech.2008.09.016>.  
709 doi:10.1016/j.jbiomech.2008.09.016.

710 [5] S. Loerakker, E. Manders, G. J. Strijkers, K. Nicolay, F. P. T. Baai-  
711 jens, D. L. Bader, C. W. J. Oomens, The effects of deformation, is-  
712 chemia, and reperfusion on the development of muscle damage during  
713 prolonged loading, *Journal of Applied Physiology* 111 (2011) 1168–  
714 1177. URL: <https://doi.org/10.1152/jappphysiol.00389.2011>.  
715 doi:10.1152/jappphysiol.00389.2011.

716 [6] A. Stekelenburg, C. W. J. Oomens, G. J. Strijkers, K. Nico-  
717 lay, D. L. Bader, Compression-induced deep tissue in-  
718 jury examined with magnetic resonance imaging and histol-  
719 ogy, *Journal of Applied Physiology* 100 (2006) 1946–1954.

720 URL: <https://doi.org/10.1152/japplphysiol.00889.2005>.  
721 doi:10.1152/japplphysiol.00889.2005.

722 [7] B. J. van Nierop, A. Stekelenburg, S. Loerakker, C. W. Oomens,  
723 D. Bader, G. J. Strijkers, K. Nicolay, Diffusion of water in  
724 skeletal muscle tissue is not influenced by compression in a rat  
725 model of deep tissue injury, *Journal of Biomechanics* 43 (2010)  
726 570–575. URL: <https://doi.org/10.1016/j.jbiomech.2009.07.043>.  
727 doi:10.1016/j.jbiomech.2009.07.043.

728 [8] W. A. Traa, M. C. van Turnhout, J. L. Nelissen, G. J. Stri-  
729 jkers, D. L. Bader, C. W. Oomens, There is an indi-  
730 vidual tolerance to mechanical loading in compression induced  
731 deep tissue injury, *Clinical Biomechanics* 63 (2019) 153–  
732 160. URL: <https://doi.org/10.1016/j.clinbiomech.2019.02.015>.  
733 doi:10.1016/j.clinbiomech.2019.02.015.

734 [9] S. Loerakker, A. Stekelenburg, G. J. Strijkers, J. J. M. Rijpkema, F. P. T.  
735 Baaijens, D. L. Bader, K. Nicolay, C. W. J. Oomens, Temporal effects of  
736 mechanical loading on deformation-induced damage in skeletal muscle  
737 tissue, *Annals of Biomedical Engineering* 38 (2010) 2577–2587. URL:  
738 <https://doi.org/10.1007/s10439-010-0002-x>. doi:10.1007/s10439-  
739 010-0002-x.

740 [10] E. Linder-Ganz, G. Yarnitzky, Z. Yizhar, I. Siev-Ner, A. Gefen, Real-  
741 time finite element monitoring of sub-dermal tissue stresses in indi-  
742 viduals with spinal cord injury: Toward prevention of pressure ul-  
743 cers, *Annals of Biomedical Engineering* 37 (2008) 387–400. URL:  
744 <https://doi.org/10.1007/s10439-008-9607-8>. doi:10.1007/s10439-  
745 008-9607-8.

746 [11] E. Linder-Ganz, N. Shabshin, Y. Itzchak, A. Gefen, As-  
747 sessment of mechanical conditions in sub-dermal tissues dur-  
748 ing sitting: A combined experimental-MRI and finite element  
749 approach, *Journal of Biomechanics* 40 (2007) 1443–1454.  
750 URL: <https://doi.org/10.1016/j.jbiomech.2006.06.020>.  
751 doi:10.1016/j.jbiomech.2006.06.020.

752 [12] E. Linder-Ganz, S. Engelberg, M. Scheinowitz, A. Gefen, Pressure–time  
753 cell death threshold for albino rat skeletal muscles as related to pres-



- 754 sure sore biomechanics, *Journal of Biomechanics* 39 (2006) 2725–  
755 2732. URL: <https://doi.org/10.1016/j.jbiomech.2005.08.010>.  
756 doi:10.1016/j.jbiomech.2005.08.010.
- 757 [13] V. Luboz, M. Bailet, C. B. Grivot, M. Rochette, B. Diot, M. Bucki,  
758 Y. Payan, Personalized modeling for real-time pressure ulcer  
759 prevention in sitting posture, *Journal of Tissue Viability* 27  
760 (2018) 54–58. URL: <https://doi.org/10.1016/j.jtv.2017.06.002>.  
761 doi:10.1016/j.jtv.2017.06.002.
- 762 [14] K. M. Moerman, M. van Vijven, L. R. Solis, E. E. van Haaften,  
763 A. C. Y. Loenen, V. K. Mushahwar, C. W. J. Oomens, On the  
764 importance of 3d, geometrically accurate, and subject-specific finite  
765 element analysis for evaluation of in-vivo soft tissue loads, *Com-  
766 puter Methods in Biomechanics and Biomedical Engineering* 20 (2016)  
767 483–491. URL: <https://doi.org/10.1080/10255842.2016.1250259>.  
768 doi:10.1080/10255842.2016.1250259.
- 769 [15] A. Macron, H. Pillet, J. Doridam, A. Verney, P.-Y. Rohan, Develop-  
770 ment and evaluation of a new methodology for the fast generation of  
771 patient-specific finite element models of the buttock for sitting-acquired  
772 deep tissue injury prevention, *Journal of Biomechanics* 79 (2018)  
773 173–180. URL: <https://doi.org/10.1016/j.jbiomech.2018.08.001>.  
774 doi:10.1016/j.jbiomech.2018.08.001.
- 775 [16] M. Bucki, V. Luboz, A. Perrier, E. Champion, B. Diot, N. Vuillerme,  
776 Y. Payan, Clinical workflow for personalized foot pressure ul-  
777 cer prevention, *Medical Engineering & Physics* 38 (2016) 845–  
778 853. URL: <https://doi.org/10.1016/j.medengphy.2016.04.017>.  
779 doi:10.1016/j.medengphy.2016.04.017.
- 780 [17] S. Niroomandi, A. Perrier, M. Bucki, Y. Payan, Real-time computer  
781 modeling in prevention of foot pressure ulcer using patient-specific finite  
782 element model and model order reduction techniques, in: *Innovations  
783 and Emerging Technologies in Wound Care*, Elsevier, 2020, pp. 87–102.  
784 URL: <https://doi.org/10.1016/b978-0-12-815028-3.00005-5>.  
785 doi:10.1016/b978-0-12-815028-3.00005-5.
- 786 [18] W. van Zwam, M. van Turnhout, C. Oomens, Risk fac-  
787 tors for developing heel ulcers for bedridden patients: A fi-

- 788 nite element study, *Clinical Biomechanics* 78 (2020) 105094.  
789 URL: <https://doi.org/10.1016/j.clinbiomech.2020.105094>.  
790 doi:10.1016/j.clinbiomech.2020.105094.
- 791 [19] S. Portnoy, I. Siev-Ner, N. Shabshin, A. Kristal, Z. Yizhar,  
792 A. Gefen, Patient-specific analyses of deep tissue loads post  
793 transtibial amputation in residual limbs of multiple pros-  
794 thetic users, *Journal of Biomechanics* 42 (2009) 2686–2693.  
795 URL: <https://doi.org/10.1016/j.jbiomech.2009.08.019>.  
796 doi:10.1016/j.jbiomech.2009.08.019.
- 797 [20] A. Dickinson, J. Steer, P. Worsley, Finite element analy-  
798 sis of the amputated lower limb: A systematic review and  
799 recommendations, *Medical Engineering & Physics* 43 (2017)  
800 1–18. URL: <https://doi.org/10.1016/j.medengphy.2017.02.008>.  
801 doi:10.1016/j.medengphy.2017.02.008.
- 802 [21] E. Ramasamy, O. Avci, B. Dorow, S.-Y. Chong, L. Gizzi, G. Stei-  
803 dle, F. Schick, O. Röhrle, An efficient modelling-simulation-  
804 analysis workflow to investigate stump-socket interaction using patient-  
805 specific, three-dimensional, continuum-mechanical, finite element resid-  
806 ual limb models, *Frontiers in Bioengineering and Biotechnol-*  
807 *ogy* 6 (2018). URL: <https://doi.org/10.3389/fbioe.2018.00126>.  
808 doi:10.3389/fbioe.2018.00126.
- 809 [22] R. M. A. Al-Dirini, M. P. Reed, J. Hu, D. Thewlis, Development and  
810 validation of a high anatomical fidelity FE model for the buttock and  
811 thigh of a seated individual, *Annals of Biomedical Engineering* 44 (2016)  
812 2805–2816. URL: <https://doi.org/10.1007/s10439-016-1560-3>.  
813 doi:10.1007/s10439-016-1560-3.
- 814 [23] M. Van Looke, C. Simms, C. Lyons, Viscoelastic prop-  
815 erties of passive skeletal muscle in compression—cyclic be-  
816 haviour, *Journal of Biomechanics* 42 (2009) 1038–1048.  
817 URL: <https://doi.org/10.1016/j.jbiomech.2009.02.022>.  
818 doi:10.1016/j.jbiomech.2009.02.022.
- 819 [24] C. K. Simms, M. V. Looke, C. G. Lyons, SKELETAL  
820 MUSCLE IN COMPRESSION: MODELING APPROACHES  
821 FOR THE PASSIVE MUSCLE BULK, *International Journal*

- 822 for Multiscale Computational Engineering 10 (2012) 143–154.  
823 URL: <https://doi.org/10.1615/intjmultcompeng.2011002419>.  
824 doi:10.1615/intjmultcompeng.2011002419.
- 825 [25] B. B. Wheatley, R. B. Pietsch, T. L. H. Donahue, L. N.  
826 Williams, Fully non-linear hyper-viscoelastic modeling of skele-  
827 tal muscle in compression, Computer Methods in Biome-  
828 chanics and Biomedical Engineering 19 (2015) 1181–1189.  
829 URL: <https://doi.org/10.1080/10255842.2015.1118468>.  
830 doi:10.1080/10255842.2015.1118468.
- 831 [26] G. Sjogaard, B. Saltin, Extra- and intracellular water  
832 spaces in muscles of man at rest and with dynamic exer-  
833 cise, American Journal of Physiology-Regulatory, Integra-  
834 tive and Comparative Physiology 243 (1982) R271–R280.  
835 URL: <https://doi.org/10.1152/ajpregu.1982.243.3.R271>.  
836 doi:10.1152/ajpregu.1982.243.3.R271, pMID: 7114288.
- 837 [27] O. A. Gimnich, J. Singh, J. Bismuth, D. J. Shah, G. Brunner, Magnetic  
838 resonance imaging based modeling of microvascular perfusion in pa-  
839 tients with peripheral artery disease, Journal of Biomechanics 93 (2019)  
840 147–158. URL: <https://doi.org/10.1016/j.jbiomech.2019.06.025>.  
841 doi:10.1016/j.jbiomech.2019.06.025.
- 842 [28] M. Argoubi, A. Shirazi-Adl, Poroelastic creep response analysis of a lum-  
843 bar motion segment in compression, Journal of Biomechanics 29 (1996)  
844 1331–1339. URL: [https://doi.org/10.1016/0021-9290\(96\)00035-8](https://doi.org/10.1016/0021-9290(96)00035-8).  
845 doi:10.1016/0021-9290(96)00035-8.
- 846 [29] M. Peyrounette, Y. Davit, M. Quintard, S. Lorthois, Multiscale mod-  
847 elling of blood flow in cerebral microcirculation: Details at capillary  
848 scale control accuracy at the level of the cortex, PLOS ONE 13 (2018)  
849 e0189474. URL: <https://doi.org/10.1371/journal.pone.0189474>.  
850 doi:10.1371/journal.pone.0189474.
- 851 [30] J. Siddique, A. Ahmed, A. Aziz, C. Khalique, A review of mix-  
852 ture theory for deformable porous media and applications, Applied  
853 Sciences 7 (2017) 917. URL: <https://doi.org/10.3390/app7090917>.  
854 doi:10.3390/app7090917.

- 855 [31] M. Hosseini-Farid, M. Ramzanpour, J. McLean, M. Ziejewski,  
856 G. Karami, A poro-hyper-viscoelastic rate-dependent consti-  
857 tutive modeling for the analysis of brain tissues, *Journal of*  
858 *the Mechanical Behavior of Biomedical Materials* 102 (2020)  
859 103475. URL: <https://doi.org/10.1016/j.jmbbm.2019.103475>.  
860 doi:10.1016/j.jmbbm.2019.103475.
- 861 [32] G. Franceschini, D. Bigoni, P. Regitnig, G. Holzapfel, Brain tis-  
862 sue deforms similarly to filled elastomers and follows consolidation  
863 theory, *Journal of the Mechanics and Physics of Solids* 54 (2006)  
864 2592–2620. URL: <https://doi.org/10.1016/j.jmps.2006.05.004>.  
865 doi:10.1016/j.jmps.2006.05.004.
- 866 [33] G. Sciumè, D. P. Boso, W. G. Gray, C. Cobelli, B. A. Schrefler,  
867 A two-phase model of plantar tissue: a step toward prediction  
868 of diabetic foot ulceration, *International Journal for Numerical*  
869 *Methods in Biomedical Engineering* 30 (2014) 1153–1169. URL:  
870 <https://onlinelibrary.wiley.com/doi/abs/10.1002/cnm.2650>.  
871 doi:<https://doi.org/10.1002/cnm.2650>. arXiv:<https://onlinelibrary.wiley.com/doi/pdf>
- 872 [34] S. Urcun, P.-Y. Rohan, W. Skalli, P. Nassoy, S. P. A. Bordas, G. Sciumè,  
873 Digital twinning of cellular capsule technology: Emerging outcomes  
874 from the perspective of porous media mechanics, *PLOS ONE* 16 (2021)  
875 1–30. URL: <https://doi.org/10.1371/journal.pone.0254512>.  
876 doi:10.1371/journal.pone.0254512.
- 877 [35] G. Sciumè, S. Shelton, W. G. Gray, C. T. Miller, F. Hussain,  
878 M. Ferrari, P. Decuzzi, B. A. Schrefler, A multiphase model for  
879 three-dimensional tumor growth, *New Journal of Physics* 15 (2013)  
880 015005. URL: <https://doi.org/10.1088/1367-2630/15/1/015005>.  
881 doi:10.1088/1367-2630/15/1/015005.
- 882 [36] G. Sciumè, Mechanistic modeling of vascular tumor growth:  
883 an extension of biot’s theory to hierarchical bi-compartment  
884 porous medium systems, *Acta Mechanica* 232 (2021) 1445–  
885 1478. URL: <https://doi.org/10.1007/s00707-020-02908-z>.  
886 doi:10.1007/s00707-020-02908-z.
- 887 [37] W. G. Gray, C. T. Miller, Introduction to the Thermody-  
888 namically Constrained Averaging Theory for Porous Medium

- 889 Systems, Springer International Publishing, 2014. URL:  
890 <https://doi.org/10.1007/978-3-319-04010-3>. doi:10.1007/978-  
891 3-319-04010-3.
- 892 [38] P. Mascheroni, C. Stigliano, M. Carfagna, D. P. Boso, L. Preziosi,  
893 P. Decuzzi, B. A. Schrefler, Predicting the growth of glioblastoma  
894 multiforme spheroids using a multiphase porous media model, *Biome-*  
895 *chanics and Modeling in Mechanobiology* 15 (2016) 1215–1228. URL:  
896 [https://doi.org/10.1007/s10237-](https://doi.org/10.1007/s10237-015-0755-0)  
897 [s10237-015-0755-0](https://doi.org/10.1007/s10237-015-0755-0). doi:10.1007/s10237-  
015-0755-0.
- 898 [39] A. J. Vaidya, B. B. Wheatley, An experimental and computa-  
899 tional investigation of the effects of volumetric boundary conditions  
900 on the compressive mechanics of passive skeletal muscle, *Journal*  
901 *of the Mechanical Behavior of Biomedical Materials* 102 (2020)  
902 103526. URL: <https://doi.org/10.1016/j.jmbbm.2019.103526>.  
903 doi:10.1016/j.jmbbm.2019.103526.
- 904 [40] M. Viceconti, S. Olsen, L.-P. Nolte, K. Burton, Extracting clin-  
905 ically relevant data from finite element simulations 20 (2005) 451–  
906 454. URL: <https://doi.org/10.1016/j.clinbiomech.2005.01.010>.  
907 doi:10.1016/j.clinbiomech.2005.01.010.
- 908 [41] I. Abaqus, Abaqus documentation, Version 6 (2014) 1–5.
- 909 [42] D. A. Sleboda, T. J. Roberts, Incompressible fluid plays a mechanical  
910 role in the development of passive muscle tension, *Biology Letters* 13  
911 (2017) 20160630. URL: <https://doi.org/10.1098/rsbl.2016.0630>.  
912 doi:10.1098/rsbl.2016.0630.
- 913 [43] B. B. Wheatley, G. M. Odegard, K. R. Kaufman, T. L. H. Donahue, A  
914 validated model of passive skeletal muscle to predict force and intramus-  
915 cular pressure, *Biomechanics and Modeling in Mechanobiology* 16 (2016)  
916 1011–1022. URL: <https://doi.org/10.1007/s10237-016-0869-z>.  
917 doi:10.1007/s10237-016-0869-z.
- 918 [44] C. Oomens, W. Zenhorst, M. Broek, B. Hemmes, M. Poeze,  
919 P. Brink, D. Bader, A numerical study to analyse the risk  
920 for pressure ulcer development on a spine board 28 (2013) 736–  
921 742. URL: <https://doi.org/10.1016/j.clinbiomech.2013.07.005>.  
922 doi:10.1016/j.clinbiomech.2013.07.005.

- 923 [45] W. A. Traa, M. C. van Turnhout, K. M. Moerman, J. L. Nelissen,  
924 A. J. Nederveen, G. J. Strijkers, D. L. Bader, C. W. J. Oomens, MRI  
925 based 3d finite element modelling to investigate deep tissue injury, *Com-  
926 puter Methods in Biomechanics and Biomedical Engineering* 21 (2018)  
927 760–769. URL: <https://doi.org/10.1080/10255842.2018.1517868>.  
928 doi:10.1080/10255842.2018.1517868.
- 929 [46] W. Lee, B. H. Won, S. W. Cho, Finite element model-  
930 ing for predicting the contact pressure between a foam mat-  
931 tress and the human body in a supine position 20 (2016)  
932 104–117. URL: <https://doi.org/10.1080/10255842.2016.1203421>.  
933 doi:10.1080/10255842.2016.1203421.
- 934 [47] M. Verver, J. van Hoof, C. Oomens, J. Wismans, F. Baai-  
935 jens, A finite element model of the human buttocks for  
936 prediction of seat pressure distributions 7 (2004) 193–203.  
937 URL: <https://doi.org/10.1080/10255840410001727832>.  
938 doi:10.1080/10255840410001727832.
- 939 [48] A. Levy, K. Kopplin, A. Gefen, Simulations of skin and  
940 subcutaneous tissue loading in the buttocks while regaining  
941 weight-bearing after a push-up in wheelchair users 28 (2013)  
942 436–447. URL: <https://doi.org/10.1016/j.jmbbm.2013.04.015>.  
943 doi:10.1016/j.jmbbm.2013.04.015.
- 944 [49] R. Sopher, J. Nixon, C. Gorecki, A. Gefen, Exposure to inter-  
945 nal muscle tissue loads under the ischial tuberosities during sitting  
946 is elevated at abnormally high or low body mass indices 43 (2010)  
947 280–286. URL: <https://doi.org/10.1016/j.jbiomech.2009.08.021>.  
948 doi:10.1016/j.jbiomech.2009.08.021.
- 949 [50] T. Zeevi, A. Levy, N. Brauner, A. Gefen, Effects of ambient  
950 conditions on the risk of pressure injuries in bedridden patients-  
951 multi-physics modelling of microclimate 15 (2017) 402–416. URL:  
952 <https://doi.org/10.1111/iwj.12877>. doi:10.1111/iwj.12877.
- 953 [51] L.-L. Gras, D. Mitton, N. Crevier-Denoix, S. Laporte, The non-  
954 linear response of a muscle in transverse compression: assessment  
955 of geometry influence using a finite element model, *Computer  
956 Methods in Biomechanics and Biomedical Engineering* 15 (2012)

- 957 13–21. URL: <https://doi.org/10.1080/10255842.2011.564162>.  
958 doi:10.1080/10255842.2011.564162.
- 959 [52] V. Klika, E. A. Gaffney, Y.-C. Chen, C. P. Brown, An overview  
960 of multiphase cartilage mechanical modelling and its role in un-  
961 derstanding function and pathology, *Journal of the Mechan-  
962 ical Behavior of Biomedical Materials* 62 (2016) 139–157. URL:  
963 <https://www.sciencedirect.com/science/article/pii/S1751616116301047>.  
964 doi:<https://doi.org/10.1016/j.jmbbm.2016.04.032>.
- 965 [53] S. C. Cowin, Bone poroelasticity, *Jour-  
966 nal of Biomechanics* 32 (1999) 217–238. URL:  
967 <https://www.sciencedirect.com/science/article/pii/S0021929098001614>.  
968 doi:[https://doi.org/10.1016/S0021-9290\(98\)00161-4](https://doi.org/10.1016/S0021-9290(98)00161-4).
- 969 [54] C. Hellmich, F.-J. Ulm, Drained and undrained poroelas-  
970 tic properties of healthy and pathological bone: A poro-  
971 micromechanical investigation 58 (2005) 243–268. URL:  
972 <https://doi.org/10.1007/s11242-004-6298-y>. doi:10.1007/s11242-  
973 004-6298-y.
- 974 [55] B. B. Wheatley, G. M. Odegard, K. R. Kaufman, T. L. H.  
975 Donahue, A case for poroelasticity in skeletal muscle fi-  
976 nite element analysis: experiment and modeling, *Computer  
977 Methods in Biomechanics and Biomedical Engineering* 20 (2016)  
978 598–601. URL: <https://doi.org/10.1080/10255842.2016.1268132>.  
979 doi:10.1080/10255842.2016.1268132.
- 980 [56] G. Sjogaard, B. Saltin, Extra- and intracellular water spaces in mus-  
981 cles of man at rest and with dynamic exercise 243 (1982) R271–  
982 R280. URL: <https://doi.org/10.1152/ajpregu.1982.243.3.r271>.  
983 doi:10.1152/ajpregu.1982.243.3.r271.
- 984 [57] M. A. Soltz, G. A. Ateshian, Experimental verification  
985 and theoretical prediction of cartilage interstitial fluid pres-  
986 surization at an impermeable contact interface in confined  
987 compression, *Journal of Biomechanics* 31 (1998) 927–934.  
988 URL: [https://doi.org/10.1016/s0021-9290\(98\)00105-5](https://doi.org/10.1016/s0021-9290(98)00105-5).  
989 doi:10.1016/s0021-9290(98)00105-5.

990 [58] Tavenas, F., Brucy, M., Magnan, J.-P., La Rochelle, P., Roy,  
991 M., Analyse critique de la théorie de consolidation uni-  
992 dimensionnelle de terzaghi, Rev. Fr. Geotech. (1979) 29-  
993 43. URL: <https://doi.org/10.1051/geotech/1979007029>.  
994 doi:10.1051/geotech/1979007029.